

Deposition of Zn_xN_y thin films and application in TFT structures

Maria Luísa Lobo Moutinho Soares de Melo

Thesis to obtain the Master of Science Degree in

Physics Engineering

Examination Committee

Chairperson: Prof. Paulo Jorge Peixeiro de Freitas

Supervisor: Prof. Reinhard Horst Schwarz

Members of Committee: Prof. António Mário Pereira Ferraz

Dr. Pedro Ricardo Charters Ribeiro da Cunha Sanguino

Dr. Rachid Ayouchi

April 2013

Agradecimentos

Este trabalho está inserido no projecto NOLEAD/PTDC/FIS/108025/2008 financiado pela Fundação para a Ciência e Tecnologia (FCT). A sua conclusão não teria sido possível sem a contribuição de diversas pessoas. A todas a elas desejo agradecer.

Em primeiro lugar, ao meu Orientador, Professor Reinhard Schwarz, por toda a paciência para responder às minhas infindáveis perguntas e por tudo o que me ensinou sobre a Física, o mundo científico e a vida em geral.

Ao Dr. Rachid Ayouchi, por todo o apoio na componente experimental deste trabalho, pela constante disponibilidade para me guiar em todas as outras fases e pela inabalável confiança e encorajamento nos momentos mais frustrantes deste trabalho.

Ao Dr. Jorge Morgado pela disponibilização da máquina de metalização e à Tânia Braz por estar disponível para a deposição dos contactos metálicos. Ao Dr. Nenad Bundaleski e ao Grupo de Ciência de Superfícies e Tecnologia de Vácuo da Universidade Nova de Lisboa pelas análises de XPS realizadas. Ao Dr. Luís Santos pela disponibilização do difractómetro de Raios-X e apoio durante essas medições. À Dr. Ana Veloso e ao Dr. Paulo Freitas pelos substratos de Nitreto de Alumínio usados neste trabalho.

Ao grupo “Lenços e Grunhidos”, por me acompanharem nestes cinco anos de noitadas quer no estudo quer nas festas. Com vocês aprendi que tudo se torna mais fácil quando se está em boa companhia. Um especial agradecimento à Rita e ao Richard pela ajuda na revisão desta dissertação.

A toda a minha família e amigos por serem a minha razão de viver. Em especial, aos meus Pais e Irmão por serem o porto seguro ao qual recolho todos os dias.

Ao Ângelo por ter estado sempre ao meu lado nestes cinco anos, por todas as horas bem passadas no Técnico e fora dele, por toda a ajuda durante a este trabalho, por nunca me deixar desanimar e por acreditar sempre em mim.

Ao meu Avô Adelino, por toda a ajuda na revisão desta tese e por ser sempre o exemplo da pessoa que um dia espero vir a ser.

A todos, o meu muito sentido obrigado!

Resumo

Os transístores são um componente fundamental da tecnologia moderna.

O presente trabalho experimental tem dois objectivos principais: estudar as condições ideais para a produção de filmes finos de Nitreto de Zinco por Deposição por Laser Pulsado e o seu posterior uso como camada semicondutora de um transistor de filme fino (TFF).

Em relação às propriedades dos filmes de Nitreto de Zinco, o nosso estudo foi centrado em dois parâmetros da deposição: o comprimento de onda do laser e a temperatura do substrato. As propriedades do filme mostraram uma grande dependência, especialmente a sua morfologia, do comprimento de onda do laser. A linha verde do laser (532 nm) foi escolhida como solução de compromisso. A temperatura do substrato também influenciou grandemente as propriedades, levando à conclusão que o Nitreto de Zinco apenas é produzido por PLD com temperaturas superiores a 350°C. Os filmes produzidos tinham uma estrutura cristalina, a altura da banda proibida foi em média 3.22 eV e a resistividade teve valores no intervalo 10^{-2} -100 $\Omega\cdot\text{cm}$. Foi também detectada uma alta percentagem de Oxigénio na superfície do filme.

Depois de algum estudo prévio, decidiu-se usar dois substratos para o TFF: AlN sobre pSi e ATO sobre ITO. A curva de saída e a curva de transferência foram medidas obtendo-se resultados com margem para optimização. O TFF fabricado com AlN+pSi como substrato teve uma melhor performance. Para este, foram estimados: threshold voltage de 1.1 V, sub-threshold swing de 1.1 V/década, rácio on/off de 10^4 e mobilidade na saturação de 0.6 cm^2/Vs .

Palavras-chave: PLD, Nitreto de Zinco, TFF, Filmes finos

Abstract

Transistors are the key component of everyday electronics, so the search for new materials and production methods becomes indispensable.

The present work has two main goals: the study of the optimal deposition conditions for the production of Zinc Nitride films by Pulsed Laser Deposition (PLD) and its later use to produce a Thin Film Transistor (TFT).

We have focused our study on two main deposition parameters: laser wavelength and substrate temperature. The film properties, particularly its morphology, showed a strong dependence on laser wavelength. The green line of a Nd:YAG laser (532 nm) proved to be the best compromise. The substrate temperature also influences the film properties leading to the conclusion that Zinc Nitride might only be PLD produced at temperatures beyond 350°C. The films showed crystalline structure, the estimated band gap was on average 3.22 eV and resistivity had a range of 10^{-2} -100 $\Omega\cdot\text{cm}$. A high percentage of Oxygen was found on the film surface, as predicted by the literature.

Three MIS structures were analysed using I-V and C-V measurements. We have decided to use two substrates for the TFT test structures: AlN on p-Si and ATO on ITO. Transfer characteristics and output characteristics measurements were undertaken. Although some optimization is necessary, we demonstrated that Zinc Nitride is a good candidate to be used as channel layer in TFT production. The AlN-based TFTs showed the best performance with threshold voltage of 1.1 V, sub-threshold voltage swing of 1.1 V/decade, an on/off ratio of 10^4 and 0.6 cm^2/Vs saturation mobility.

Keywords: PLD, Zinc Nitride, TFT, Thin Films

Contents

Agradecimientos.....	i
Resumo.....	iii
Abstract.....	v
Contents.....	vii
List of Tables.....	xi
List of Figures.....	xiii
List of Abbreviations.....	xv
Chapter 1 - Introduction.....	1
Chapter 2 - Literature Review.....	3
2.1 Pulsed Laser Deposition (PLD).....	3
2.1.1 PLD Introduction.....	3
2.1.2 PLD Operation.....	4
2.2 Zinc Nitride (Zn_3N_2): Properties and Production Methods.....	7
2.2.1 Zn_3N_2 Production by PLD.....	7
2.2.2 Zn_3N_2 Production by other methods.....	8
2.3 Metal Insulator Semiconductor Structures (MIS).....	9
2.3.1 Capacitance-Voltage Characteristic (C-V).....	10
2.3.2 Current-Voltage Characteristic (I-V).....	12
2.3.3 MIS used.....	13
2.4 Thin Film Transistors (TFT).....	13
2.4.1 Mode of Operation.....	14

2.4.2 Non-ideal TFTs	17
2.4.3 TFT Performance Evaluation	17
2.4.4 TFT with ZnO, Zn ₃ N ₂ and ZnON	18
Chapter 3 - Experimental Methods	21
3.1 Pulsed Laser Deposition	21
3.1.1 Apparatus.....	21
3.1.2 Experimental Procedure	22
3.2 Thermal vaporization	23
3.3 I-V Measurements	23
3.3.1 Instrumentation	23
3.3.2 Program	24
3.4 Transmission	25
3.5 C-V Measurements.....	27
3.6 Scanning Electron Microscopy (SEM)	28
3.7 X-Ray Diffraction (XRD).....	29
3.8 X-Ray Photoelectron Spectroscopy (XPS)	30
Chapter 4 - Results on Zn ₃ N ₂ Film Deposition	33
4.1 Film Properties versus Laser Wavelength	34
4.1.1 Morphology	34
4.1.2 Optical Properties.....	37
4.1.3 Electrical Properties	37
4.1.4 Conclusion	38
4.2 Film Properties versus Substrate Temperature	39
4.2.1 Morphology	39
4.2.2 Optical Properties.....	43
4.2.3 Structure	45
4.2.4 Electrical Properties	47
4.3 Oxygen Contamination	48
Chapter 5 - Results on MIS and TFT Production	51

5.1 MIS results	51
5.1.1 I-V Characteristics	52
5.1.2 C-V Characteristic	52
5.1.3 MIS choice	53
5.2 Zinc Nitride Deposition Conditions	53
5.3 Contact geometry	54
5.4 TFT structure.....	54
Chapter 6 - Results on TFT Operation.....	55
6.1 TFT on ATO+ITO Substrate.....	56
6.1.2 Output characteristics.....	56
6.1.2 Transfer characteristics	57
6.2 TFT on AlN+Si-2 Substrate.....	58
6.2.1 Output characteristics.....	58
6.2.2 Transfer characteristics	60
Chapter 7 - Conclusion and Future Work.....	63
7.1 Conclusion	63
7.2 Future Work.....	64
Appendix A - I-V Measurements Program - Flowchart	65
References	67

List of Tables

Table 4.1 – Laser wavelength and deposition duration each sample.....34

Table 4.2 – Resistivity for different laser wavelengths.....38

Table 4.3 – Substrate temperature during deposition of each sample39

Table 4.4– Estimated grain size variation with the temperature.....41

Table 4.5 – Energy gap determined with the Tauc method45

Table 4.6 – Sample surface composition.....49

Table 4.7 – Sample composition before and after sputtering.....49

List of Figures

Figure 2.1 – Pulsed Laser Deposition apparatus	4
Figure 2.2 – Film growth modes: a) Island growth b) Layer-by-layer growth c) Island growth on top of monolayers	6
Figure 2.3 – Zn_3N_2 crystal structure [19]	7
Figure 2.4 – MIS structure in the Flat-band region	10
Figure 2.5 – MIS structure in the different regions: a) accumulation b) depletion c) inversion	11
Figure 2.6 – Conduction mechanisms through MIS structures [41]: a) direct tunnelling b) Fowler-Nordheim tunnelling c) thermionic emission d) Frank-Poole emission	12
Figure 2.7 – TFT classification: a) coplanar bottom-gate, b) staggered bottom-gate, c) coplanar top-gate and d) coplanar top-gate	14
Figure 2.8 – TFT circuit configuration	15
Figure 2.9 – Output characteristic of a FET [41].....	17
Figure 2.10 – a) Output and b) Transfer characteristics of ZnO TFTs [45].....	18
Figure 2.11 – TFT with ZnO channel layer deposited by PLD: a) output characteristic b) transfer characteristics.....	19
Figure 2.12 – Comparison of $Zn_3N_2/ZnON$ TFTs reported in the literature: a) [18] b) [47] c) [29].....	20
Figure 3.1 – Part of our Pulsed Laser Deposition apparatus	21
Figure 3.2 - I-V measurements circuit.....	23
Figure 3.3 – PC-Instruments communication with the interface.....	24
Figure 3.4 - Experimental setup for the optical measurements.....	26
Figure 3.5 - Xenon lamp spectrum	27
Figure 3.6 - C-V measurements circuit	28
Figure 3.7 – X-Ray diffraction on a crystal structure.....	30
Figure 4.1 - Plasma plume during a Zinc Nitride deposition	33
Figure 4.2 - SEM images with 1000x magnification for different laser wavelengths: a) 266 nm, b) 532 nm and c) 1064 nm.....	34
Figure 4.3 - SEM images with 50,000x magnification for different laser wavelengths: a) 266 nm, b) 532 nm and c) 1064 nm.....	35
Figure 4.4 – Quartz window Transmittance spectrum as removed and cleaned with ethanol and HF..	36

Figure 4.5 – Transmittance spectrum for different laser wavelengths: a) 266 nm, b) 532 nm and c) 1064 nm.	37
Figure 4.6 – I-V curves for different laser wavelengths: a) 266 nm, b) 532 nm and c) 1064 nm.	38
Figure 4.7 – SEM images at 1000x magnification for different substrate temperatures: a) 100°C, b) 200°C, c) 300°C, d) 350°C, e) 400°C and f) 500°C.....	40
Figure 4.8 – Target-originated particulates	41
Figure 4.9 - SEM images at 50,000x magnification for different substrate temperatures: a) 100°C, b) 200°C, c) 300°C, d) 350°C, e) 400°C and f) 500°C.....	42
Figure 4.10 – Transmittance spectrum for different substrate temperatures: a) 100°C, b) 200°C, c) 300°C, d) 350°C, e) 400°C and f) 500°C.....	43
Figure 4.11 – Application of Tauc method to the ZnN34 transmission data	44
Figure 4.12 – Absorption Plot for different substrate temperatures: a) 100°C, b) 200°C, c) 300°C, d) 350°C, e) 400°C and f) 500°C	44
Figure 4.13 - XRD spectrum for different substrate temperatures: a) 100°C, b) 200°C, c) 300°C, d) 350°C, e) 400°C and f) 500°C	46
Figure 4.14 – Crystal size variation with the substrate temperature.....	47
Figure 4.15 – Resistivity temperature dependence	47
Figure 4.16 – XPS spectrum for substrate temperature of 300°C	48
Figure 4.17 - XPS spectrum for substrate temperature of 300°C before sputtering, after 20 cycles and after 40 cycles of sputtering.....	49
Figure 5.1 – MIS structures: a) Al+ATO+ITO b) Al+AlN+Si – 1/2	51
Figure 5.2 – Transversal I-V Curves of the MIS structures.....	52
Figure 5.3 – C-V curves of the MIS structures	53
Figure 5.4 – Source and Drain contact geometry.....	54
Figure 5.5 – TFT test structures configuration	54
Figure 6.1 – Optical Microscope images of the Source and Drain contacts a) ATO+ITO substrate b) AlN+Si substrate.....	55
Figure 6.2 - Output Characteristics of the TFTs: a) ATO400 b) ATO450	56
Figure 6.3 – Square-root Transfer Characteristics at saturation of the TFTs: a) ATO400 b) ATO450..	57
Figure 6.4 - Logarithmic Transfer Characteristics at saturation of the TFTs: a) ATO400 b) ATO450...	58
Figure 6.5 – Output Characteristics of the TFTs: a) AlN400 b) AlN450.....	59
Figure 6.6 – Square-Root Transfer Characteristic at the saturation region of the TFTs: a) AlN400	60
Figure 6.7 – Logarithmic Transfer Characteristic at the saturation region of the TFTs: a) AlN400.....	61

List of Abbreviations

ATO - Aluminium-Titanium Oxide

BJT – Bipolar Junction Transistor

ITO - Indium-Tin Oxide

C-V – Capacitance-Voltage Curve

FET – Field-Effect Transistor

IR – Infrared

I-V – Current-Voltage Curve

MOSFET - Metal-Oxide Semiconductor Field-Effect Transistor

MIS – Metal-Insulator-Semiconductor structure

PLD – Pulsed Laser Deposition

SEM – Scanning Electron Microscopy

TFT – Thin Film Transistor

UV – Ultraviolet

XRD – X-ray Diffraction

XPS – X-ray Spectroscopy

Chapter 1

Introduction

Zinc Nitride (Zn_3N_2) is a group II-V compound semiconductor. This is still a poorly known semiconductor with reported shifting properties, depending on the production method. It has recently drawn the attention of a number of research groups, including ours. Several production methods have been used such as: Molten Salt Electrochemical Process, Molecular Beam Epitaxy (MBE), Filtered Cathodic Vacuum Arc Deposition, Plasma-assisted Metal Organic Chemical Vapour Deposition and, predominately, RF Assisted Magnetron Sputtering and, our focus, Pulsed Laser Deposition (PLD). It is a hot topic in materials science, with several articles published in the last couple of years. Properties like the optical band gap are yet to be established by the scientific community with new results cropping up recently.

Zinc Nitride is a promising semiconductor to use in electronic and optoelectronic applications (photovoltaic, sensors, TFTs and so on) owing to low cost and ecological friendliness. The high availability of its composing materials is also appealing.

A significant part of modern technology owes its development to the invention and implementation of the Metal-Oxide Semiconductor Field-Effect Transistor (MOSFET). The first device resembling a transistor was a Metal-Semiconductor Field-Effect Transistor (MESFET) and was first described in 1930 by J. E. Lilienfeld and O. Heil [1]. The MISFET was later on patented by the same authors [2]. However, at the time there was neither sufficient scientific knowledge nor technological know-how to manufacture this kind of device. So, the first MOSFET was only developed for practical use in 1960 by D. Kahng and M. M. Atalla [3]. This device represented an extremely important breakthrough in technology as it offered more miniaturization, lower cost and operating lifetime than the vacuum tube that was in use at the time. Transistors are commonly used as amplifiers and switches in several electronic applications.

Thin Film Transistors (TFT) are field effect transistors (FET) and their structure and operation principles are similar to those of the MOSFET. However, there are some important differences to consider: TFT frequently uses an insulation substrate, the production temperatures are usually lower

and the absence of p-n junctions in the Drain and Source contacts, which leads to a slightly different mode of operation.

The first Thin Film Transistor (TFT) was produced in 1962 by P. K. Weimer who used n-type polycrystalline Cadmium Sulphide (CdS) as a channel and silicon monoxide as insulator [4]. An important breakthrough in this field occurred in 1979 with the production of the first functional TFT made from hydrogenated amorphous silicon (a-Si:H). Since then, the development of these devices has drawn the attention of numerous research groups and companies. There is a constant search for new materials and production methods. In the last decade, a new impulse has been given to this research field especially in areas such as the transparent and organic TFTs. The use of binary compounds, such as Zinc Oxide, as the channel layer has been extensively studied since the 2000's decade. The high mobility achieved is the major advantage of this kind of device.

Some of the possible TFT applications include integrated displays, photovoltaics, light sensors, smart labels, lightning, and integrated logic devices.

This work focuses on the Pulsed Laser Deposition of Zinc Nitride thin films and its possible use as the semiconductor layer of a Thin Film Transistor (TFT). An auxiliary program was specifically built on the Labview 8.6 platform to perform the Current-Voltage (I-V) measurements needed in this work. Several other characterization methods were used: transmission, SEM, C-V, XRD and XPS.

This experimental work was done at the Physics Department of Instituto Superior Técnico, Lisbon, Portugal. The work was supervised by Professor Reinhard Schwarz and Dr. Rachid Ayouchi. PLD depositions, I-V, C-V and transmission measurements were obtained using the research group infrastructure available at the Physics Department. XRD and SEM were done with a diffractometer of the ICEMS group. XPS analysis was carried out at the Physics Department of Universidade Nova de Lisboa by the "Ciência de Superfícies e Tecnologia de Vácuo" group.

This Dissertation is divided in seven chapters. This introduction is the first chapter. The second chapter covers a PLD, Zinc Nitride and TFT production literature review. In the third chapter the experimental methods used in this work are described. In the fourth chapter, the influence of two PLD parameters (laser wavelength and substrate temperature) on the deposited Zinc Nitride films is analysed. In the fifth chapter, three Metal-Insulator-Semiconductor (MIS) structures are studied so as to choose the best suitable substrates to use in the TFT test structures production. It is also established the Zinc Nitride deposition parameters to use in the following step. In the sixth chapter the TFT performance is studied and compared to those reported in the literature. In the seventh chapter the conclusions of this work are presented as well as some suggestions for future work to do on this subject.

Part of the experimental results from this work will be showed at a poster presentation at the EMRS 2013 conference, in Strasbourg, France with the title: *Reactive Pulsed Laser Deposition of Zinc Nitride thin films*.

Chapter 2

Literature Review

2.1 Pulsed Laser Deposition (PLD)

2.1.1 PLD Introduction

Pulsed Laser Deposition (PLD) is a physical vapour deposition technique. The basic concept behind this method is to evaporate a small part of a material by impinging a high power laser pulse onto a target.

Pulsed Laser Deposition was made possible after the invention of the first laser in 1960 by Theodore Maiman. In 1965 a ruby laser was used by A. H. Smith and A. F. Turner to deposit semiconductor and dielectric thin films [5]. This marks the beginning of PLD usage as a production method. The first practical installations appeared in the early 1980's and the first good results with this method appeared within that decade. In the 1990's, laser technology developed fast such as reliable Q-switched lasers and lasers with high repetition rates, which provided a strong progress in the PLD technique.

The PLD technique allows preparing several materials such as semiconductors oxides, nitrides and carbides, superconductors, ferroelectrics and metallic systems.

There are three main types of PLDs: conventional, inert gas and reactive. In the conventional PLD the deposition is done with vacuum and the material ablated from the target deposit directly on the substrate. In the inert gas PLD, an inert gas such as Xenon or Argon is used as background gas. The reactive PLD uses a reactive gas background to allow the interaction between the ablated material and the gas forming new chemical species. In this thesis the Reactive PLD was used.

PLD has a set of advantages such as: it is versatile as it can be used to deposit different materials with different gases; it is cost-effective given that the same laser can be used for several experimental apparatus; it is fast with the possibility of depositing quality samples within a few minutes, depending on the laser power; it allows an easy control of the deposited thickness and a stoichiometric deposition of the target and it is scalable.

However, it has some disadvantages as, for instance, the possible presence of particles in the film, the target surface modification, the non-uniformity of the deposition area and the unintentional sputtering of the substrate surface.

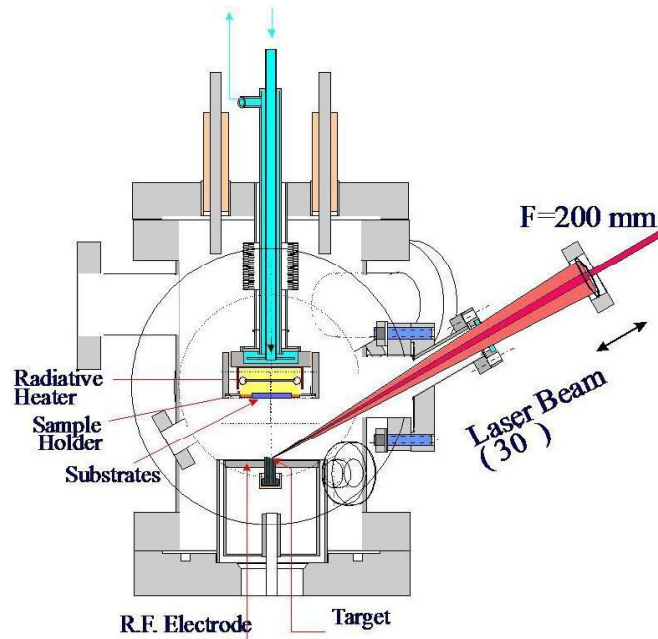


Figure 2.1 – Pulsed Laser Deposition apparatus

2.1.2 PLD Operation

An optical system focuses a high power laser and enters the deposition chamber through a viewport. It then travels through the chamber and hits the target, evaporating part of it. The evaporated material subsequently interacts with the environmental gas and deposits on the substrate. The deposition process may be split into four main stages: laser-target interaction, gas phase transportation, deposition and nucleation and film growth.

Laser target interaction stage

In the laser target interaction phase, when the laser beam with sufficiently high energy density hits the target, the absorption of its electromagnetic energy causes the melting and evaporation of the material. If the photons have sufficiently high energy, chemical bonds of the material are also broken. The penetration depth of the laser in the target depends both on its wavelength and on the material itself.

Two kinds of particles may appear on the films when Pulsed Laser Deposition is used: particulates and precipitates. Particulates have rounded shapes and micrometric size. These particles are difficult to eliminate when using PLD. Precipitates have a nanometric size and irregular shape. The predominance of either the particulates or the precipitates depends on the deposition conditions. The spatial distribution of these structures is typically irregular. The density of particulates increases with the number of laser pulses. This is a critical problem for the film quality and device operation as it can induce a high non uniformity and generate short-circuits across the film.

The precipitates are formed in the gas-material interaction step and are caused by the gas phase condensation of the evaporated material. These particles appear in most deposition methods such as PLD, Sputtering and Chemical Vapour Deposition.

The particulate formation was first explained by the subsurface heating effect [6]. However, further studies demonstrated that there is a severe target surface morphology modification during the deposition. The irregularities in the surface cause a non uniform absorption of the laser light, which increases the deposition of particulates in the film. It is thus recommended to polish the target surface before starting the deposition. The absorption of the laser light is as well influenced by the thermal and optical properties of the target so a densely packed target and the use of a short wavelength are recommended [7]. Metallic targets have shown a greater tendency to form particulates. This happens because these materials have a high thermal conductivity, hence when the laser impinges on the surface, it may form segregates, which solidify rapidly and may be later ablated and deposited on the film. It has also been demonstrated that the laser energy density is an important factor in this matter [8].

Gas phase transportation stage

In this stage, initially a thin layer of partly ionized plasma (plume) on the target surface is formed and is composed by neutral atoms, ions and electrons. Given that the pressure of this plume is much higher than that of a typical background gas, the plume will expand rapidly. The visible light of the plume is due to fluorescence and recombination processes in the plasma. The plume behaves in a different manner in vacuum and in the presence of an ambient background gas. Since in this work we used Reactive Pulsed Laser Deposition, the interaction between the plume and the background gas will be analysed.

As the plume interacts with the background gas, it loses kinetic energy, changes its spatial distribution mainly by scattering processes. The kinetic energy loss and plume broadening increase with increasing gas pressure due to a higher collision probability. For intermediate gas pressures, if the species have sufficiently high kinetic energy, they are able to pass through without suffering a significant amount of collisions arriving to the substrate with high kinetic energy. For higher background pressures, the species loses a significant amount of kinetic energy and diffuse into the substrate with a low speed [9].

The material-gas interaction also leads to the formation of new chemical bonds. This process is made possible by the dissociation of the background gas molecules and their interaction with the target ablated materials leading to the formation of new chemical species.

The background pressure, the target to substrate distance and the substrate temperature deeply influence the processes occurring at this stage.

Deposition stage

In this stage, the ablated species reach the substrate surface, lose their kinetic energy and deposit on it. However, if the species hit the surface with too high kinetic energy, they cause the sputtering of the previously deposited film and of the substrate. A collision region is thus formed where the incident

and sputtered species interact, allowing their condensation and subsequent deposition on the substrate. The condensation rate has to be higher than the sputtering rate to have an effective film deposition.

The unintentional film/substrate sputtering may cause severe damage to the substrate and substrate-film interface. Experiments reported in the literature showed a high density of particle implantation on the substrate-film interface originated in the deposition with metallic targets. Metallic interfaces are thus formed causing unwanted sheet conductivity in theoretical insulator substrates. The sheet conductance showed a high dependence on the background gas pressure and a variation of up to 6 orders of magnitude [10].

Furthermore, particles originated in metallic targets were proven to induce a preferential sputtering leading to non-stoichiometric film composition. Indirect deposition and low laser fluence were reported to be possible solutions for this problem [11]. Also, high background gas pressures have shown to have an important role in the reduction of damages caused by target ablated species on the substrates [12].

Nucleation and film growth stage

As the deposited species (adatoms) arrive to the substrate, they diffuse through several atomic distances until the thermodynamic equilibrium is reached. Film growth may be divided into three different modes: island growth, layer-by-layer growth and island growth on top of monolayers.

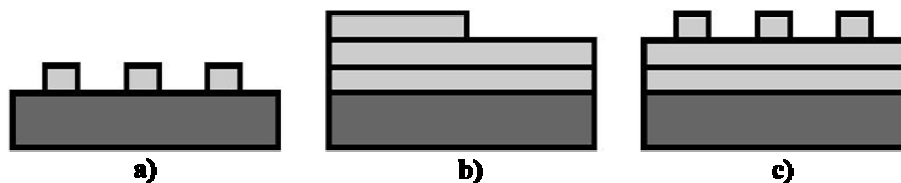


Figure 2.2 – Film growth modes: a) Island growth b) Layer-by-layer growth c) Island growth on top of monolayers

In the three-dimensional island growth, as the ablated species arrive, mobile islands begin to form. As more material arrives, it deposits on top of those islands increasing their size and making them coalesce together. This growth mode occurs when atoms or molecules in a growing film are more strongly bound to each other than to the substrate. Low substrate temperature and high deposition rate induce this kind of film growth.

In the layer-by-layer growth, the nuclei formed diminish in size and join together forming uniform monolayers of material. This growth mode requires adatoms with high mobility and a good lattice match between the film and the substrate. Higher temperatures and lower deposition rates also favour this growth mode.

In the third mode, islands are formed on top of initially layer-by-layer grown films. This phenomenon is often caused by the mismatch between the substrate and film lattices. So, as the film grows and its thickness increases, small islands are formed on top of previously deposited monolayers which have a rough surface.

The nucleation and film growth stage is mainly influenced by the interfacial energies, the substrate temperature and the crystal structures. The substrate temperature is important to ensure a sufficient surface mobility of the arriving species.

2.2 Zinc Nitride (Zn_3N_2): Properties and Production Methods

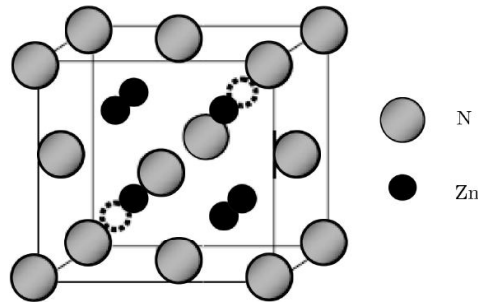


Figure 2.3 – Zn_3N_2 crystal structure [19]

Zinc Nitride (Zn_3N_2) is a group II-V compound semiconductor with cubic antixynte structure, the lattice constant of which is $a = 9.78(1) \text{ \AA}$ and its crystal structure is shown in Figure 2.3. Zinc Nitride powder was first reported to be produced in 1940 by H. Juza and Z. Hahn [13]. Zinc Nitride thin films were first produced by K. Kuriyama, Y. Takahashi and F. Sunohara in 1993 by the direct reaction between ammonia (NH_3) and metallic Zinc [14]. Zinc Nitride has in the recent years drawn the attention of several research groups. The results, however, have been very scarce so far. In particular, reports differ strongly concerning the compound band gap, which has shown dependence on the production method. This fact makes the Zinc Nitride a still poorly understood material that requires further research. A brief summary of the production methods previously employed and respective Zinc Nitride properties will be presented further on.

2.2.1 Zn_3N_2 Production by PLD

The PLD technique has been successfully used in the production of several Nitride compounds such as Aluminium Nitride (AlN) and Gallium Nitride (GaN) [15]. However, to our knowledge, the deposition of Zinc Nitride by PLD has not yet been extensively studied. It has only been produced by S. Simi *et al.* [16] and our group either RF-Assisted [17,18] or not [19]. A range of different properties of the Zinc Nitride films were reported.

Concerning the optical properties, results were similar as far as the main parameter, the energy gap is concerned. The band gap was reported to be direct and its value varied from 3.2 to 3.5 eV [16-19]. The optical transmittance beyond the band gap was around 85% [17-19] or variable with the Nitrogen pressure from ~75% to ~100% [16].

The X-Ray peaks seen were observed at 34.2° and 36.8° [16-19]. The films showed an amorphous structure at low Nitrogen pressures and polycrystalline at higher pressures [16]. These values correspond to the known peaks of the Zinc Nitride crystal structure.

The morphology reported sub-micrometer crystallites distributed discontinuously over the film surface with grain sizes of ~20-60 nm [16]; ~ 30-50 nm [19] and from 10 to 30 nm with the presence of particulates with diameter of 0.2 to 2 μm in the film [17,18].

2.2.2 Zn₃N₂ Production by other methods

Several other methods were used to produce this material such as Molten Salt Electrochemical Process [20], Molecular Beam Epitaxy (MBE) [21], Filtered Cathodic Vacuum Arc Deposition [22], Plasma-assisted Metal Organic Chemical Vapour Deposition [23] and, predominately, RF-assisted Magnetron Sputtering [25-36]. The respective properties are very different among them and with the ones observed in PLD. Parameters such as the substrate temperature, the Nitrogen pressure/fraction and the target used strongly influence the film properties.

Morphology

Concerning the film morphology, there is no agreement in the literature in how the growth conditions influence the morphology and grain size of the films. Either no dependence was detected [24] or it was reported that the grain size increased when increasing the substrate temperature from 125°C to 200°C [25]. Either way, the films were reported to be crack free and densely packed. Recent results, achieved with Sputtering, have shown a curious flower-like morphology when the deposition was done with an Ar-N₂ mixture [26].

Optical Properties

Regarding the optical properties of this material, there is a strong discrepancy between the results reported. The material is generally said to be a direct semiconductor. The optical band gap has a high inconsistency between the obtained values with two groups of values: 1.01-1.47 eV [20,24,25,27-29] and 3.2 eV [22,30,31]. Some reports indicate a decrease of the band gap with increasing substrate temperature [25]. An indirect band gap has also been reported with band gap 2.12 eV [31].

The transmittance of photons with energies above the band gap has also a strong variation: ~60-90%. The transmittance in this region was said to increase with the increase of Nitrogen fraction, to increase with increasing substrate temperatures [24] and to be dependent on the film thickness [30].

Structural Properties

Most research groups study the crystal structure of Zinc Nitride using the X-Ray Diffraction (XRD) method. Every group [20,22,24,26-30,33] reported highly crystalline films with the peaks according to the known peaks of Zinc Nitride established by the Joint Committee on Powder Diffraction [34]. The most reported peaks are the 2 θ angles: 34.4° that corresponds to the (321) Miller plane and 36.8° that corresponds to (400) plane. Both of these peaks exist in the antibixyte crystal structure. However, the (400) peak is also observed in the metallic Zinc diffraction pattern [35]. It was also reported that higher substrate temperatures and Nitrogen pressures induce more crystalline films [24,27,29].

Electrical Properties

The electrical properties of this material have also been studied. Resistivity values are reported in the range of 10^{-3} - 10^{-1} Ω .cm. A strong dependence on the substrate temperature has been described increasing from RT to 100°C and decreasing for higher temperatures [24,25]. The carrier mobility of Zinc Nitride films was reported to have a range of 10^{-1} -100 $\text{cm}^2 \text{V}^{-1} \text{s}^{-1}$ [24,25,27,29,30,32]. Hall measurements reported n-type films [24,25,29,30,32].

Metallic contacts done with Al, Au and Cu have been studied as potential ohmic contacts for Zinc Nitride films. All three elements showed good ohmic behaviour [27].

Oxygen contamination

Oxygen contamination has been extensively reported as a common Zinc Nitride production issue. Zinc Nitride is a hydrophilic material [29], which means it has the tendency to absorb the water vapour present in the atmosphere. Also, Oxygen is more reactive than Nitrogen because of their different electronic properties. These two facts make very probable the contamination of Oxygen in Zinc Nitrides films. The Oxygen may thus combine with Zinc atoms forming Zinc Oxide (ZnO), Zinc Oxynitride (ZnON) and $\text{Zn}(\text{OH})_2$ structures. This phenomenon has been studied by several groups using techniques like XPS, RBS, EDS and Ellipsometry [20,24,29,33].

The contamination of the Oxygen in the Zinc Nitride surface has been detected from down to a few dozen nanometres into the film [20,24,29] or to expand over time to every layer of the film [33]. Also, XPS peaks reported are coherent with OH-Zn, H-Zn, N-Zn bonds [24,29]. However, the use of XPS as analytical method brings a well known problem in detecting Nitrogen. It has been observed that Ar-ion sputtering, usually used to remove the first layers of the sample, removes preferably Nitrogen atoms introducing a systematic error in these measurements [37,38]. The oxidation process was observed to be less dominant for higher substrate temperatures [33]. The presence of Oxygen on Zinc Nitride films and its combination with Zinc forming Zinc Oxide, Zinc Oxynitride and $\text{Zn}(\text{OH})_2$ may thus alter significantly the properties of the films. The intentional incorporation of Oxygen in Zinc Nitride films as also been studied to produce p-type semiconductors [36].

The discrepancy in the reported band gaps has thus been explained by this presence of Oxygen in the films, which causes the formation of, among others, Zinc Oxide at the surface and may increase the band gap of the film to values near 3.3 eV [39]. Concerning the structural properties, since the Zinc Nitride 34.4° peak is very close to the 34.1° peak of the Zinc Oxide wurtzite structure, these peaks may easily be mislabelled [40]. Hence, XRD should not be used as the only method to differentiate these materials.

2.3 Metal Insulator Semiconductor Structures (MIS)

The Metal Insulator Semiconductor (MIS) structure is the basic component of any FET. Silicon Oxide on Silicon (SiO_2/Si) structures are the most widely used MIS and are the base structure of MOSFETs. Research for alternative materials has increased in the last decades with Transparent Conductive Oxides (TCOs) as important substitute candidates.

The following sections were written using [41] and [42] as references, which may be consulted for further information.

2.3.1 Capacitance-Voltage Characteristic (C-V)

Applying a voltage (positive or negative) to the metal layer of the MIS greatly influences the band structure. The following analysis will be done for a Metal-Insulator-Semiconductor structure with an n-type semiconductor. The basic ideal case will be analysed and possible influence from defects will be taken into consideration later.

When the three components are joined and the equilibrium is reached, as established by the principle of invariance of the Fermi level, the semiconductor Fermi level and those of the metal align themselves. The structure is in the Flat-Band condition. The band structure is presented in Figure 2.4.

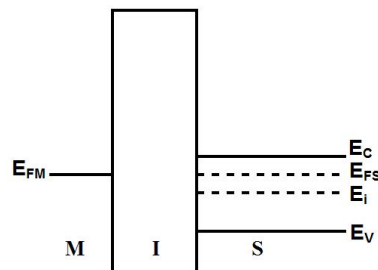


Figure 2.4 – MIS structure in the Flat-band region

Accumulation

Positive charges are introduced on the metal surface when a positive voltage is applied to it and this induces an electric field (\vec{E}) across the dielectric. This field attracts the electrons (majority carriers) to the semiconductor surface. The MIS is in the accumulation region (Figure 2.5a). The conduction band gets close to the Fermi level with the presence of electrons in the accumulation region. As the Fermi level has to be invariant, the band bends downwards to accommodate these changes. The MIS capacitance in accumulation is given by the capacitance across the insulator (C_i).

Depletion

When a negative voltage is applied, negative charges emerge at the metal surface. The electrons are therefore repelled off the semiconductor surface leaving uncompensated donors. This creates a positive depletion region at the semiconductor surface. The absence of electrons in the depletion region causes the Fermi level to be pushed away from the conduction band. For that to happen, the bands are bent upwards. See Figure 2.5b). The capacitance in this region is the series combination of the insulator capacitance with the depletion region capacitance.

Inversion

When a stronger negative voltage is applied, besides creating the depletion layer, it attracts the holes (minority carriers) to the semiconductor surface, see Figure 2.5c). In this operation region, the band bending is so strong that the Fermi level is below the intrinsic level and the semiconductor is

locally p-type, forming an inversion layer. With a further negative voltage, there is a higher concentration of holes at the surface until it saturates and the depletion layer remains constant, the device is then in strong inversion.

The voltage required for the device to be in strong inversion, threshold voltage (V_T), is:

$$V_T = \frac{Q_d}{C_I} + 2\phi_F \quad (2.1)$$

where Q_d is the charge per unit area in the depletion region at strong inversion and ϕ_F is the surface potential.

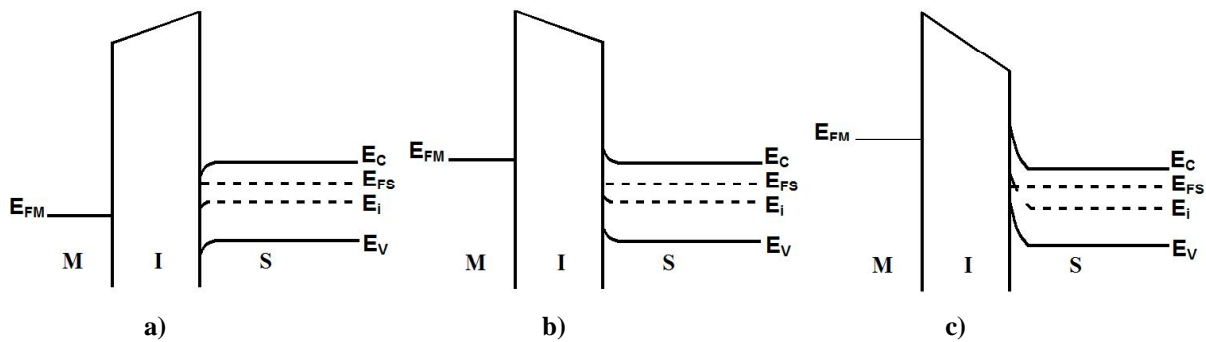


Figure 2.5 – MIS structure in the different regions: a) accumulation b) depletion c) inversion

Non-ideal MIS

The previous analysis was made assuming that we have an ideal MIS structure, but that is not a real life case MIS. Three facts may be responsible for this: there is either a work function difference, there are interface charges or, third fact, there are charges trapped inside the insulator film.

The first one occurs when there is a work function difference between the semiconductor and the metal. In that case, an electrical flow between the metal and the semiconductor is required to have a constant Fermi level. This implies band bending at equilibrium so voltage has to be applied to reach the flat band condition

The presence of charges is also an important fact to take into account. These charges can either be inside the insulator or at the semiconductor-oxide interface. The first case is usually the result of defects in the dielectric that induce the presence of charges at the semiconductor surface. There can also be interface charges caused by a sudden termination of the crystal at the insulator surface or originated during the manufacturing process. To reach a flat band condition, voltage must be applied as well as a band bending just as in the case of work function difference.

The voltage required for the MIS to be in the flat-band condition is the following:

$$V_{FB} = \Phi_{ms} - \frac{Q_I}{C_I} \quad (2.2)$$

where Φ_{ms} is the work function difference between the metal and the semiconductor and Q_i is the total charge present at the interface. Thus, the condition for strong inversion changes from Eq. 2.1 to the following:

$$V_T = \Phi_{ms} - \frac{Q_I}{C_I} + \frac{Q_d}{C_I} + 2\phi \quad (2.3)$$

2.3.2 Current-Voltage Characteristic (I-V)

An ideal insulator does not allow any current to flow through it. However, in real insulators used as device components, there is always some leakage of current that can substantially influence the device performance. There are several processes that can cause current flow through the insulator [41]:

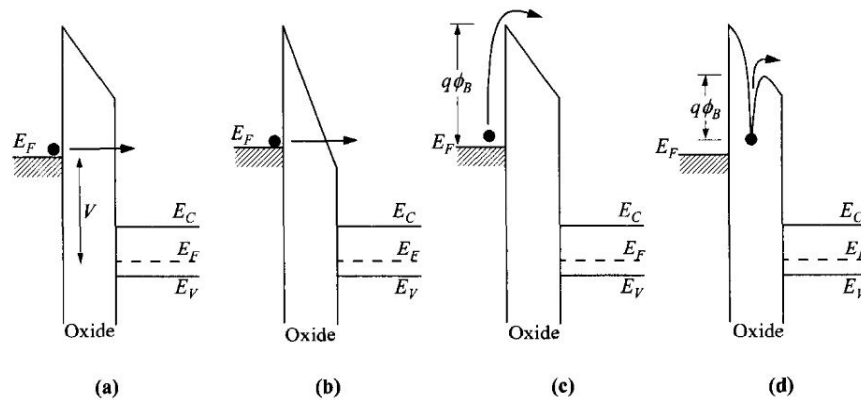


Figure 2.6 – Conduction mechanisms through MIS structures [41]: a) direct tunnelling b) Fowler-Nordheim tunnelling c) thermionic emission d) Frank-Poole emission

Tunnelling effect - explained by quantum mechanics, that tells us that electrons with less energy than the potential barrier created by the insulator can tunnel through it. This effect can happen either directly through the full thickness of the insulator (direct tunnelling) or only through a part of it (Fowler-Nordheim tunnelling) and is much dependent on voltage.

Thermionic emission - occurs if the electron has sufficient thermal energy to hop over the potential barrier created by the insulator.

Frenkel-Poole emission: caused by the emission of the electrons trapped in the insulator into its conduction band.

Ohmic conduction effect - happens when, at high temperatures, the electrons have sufficient energy to hop from one isolated state of the insulator to the other.

Ionic conduction - occurs when, after a prolonged application of electric field, the resulting ions at the interfaces move back to their previous positions. This process is one of the causes of hysteresis that may appear in an I-V characteristic.

Space-charge limited conduction - originated by the charges present in the insulator that are not compensated by positive charges.

Because of all the effects mentioned above, the thickness of the dielectric cannot be reduced beyond a certain point or else the leakage current will become a serious problem. Irregularities and defects in these materials have also a strong influence in this issue. Persistent charge flow through the dielectric might irreversibly damage and spoil the material.

2.3.3 MIS used

Three MIS structures will be studied in this work: two with Aluminium, Aluminium Nitride p-type Silicon and one with Aluminium, Aluminium-Titanium Oxide (ATO) and Indium-Tin Oxide (ITO).

Aluminium + Aluminium-Titanium Oxide (ATO) + Indium-Tin Oxide (ITO)

Aluminium-Titanium Oxide (ATO) with Indium-Tin Oxide (ITO) structures have been widely used to take advantage of their optical properties. Both of these materials are wide band gap semiconductors and thus highly transparent to the visible light. For this reason, ATO+ITO structures are very suitable for optoelectronic and photovoltaic applications.

Aluminium-Titanium-Oxide (ATO) is a wide band gap n-type semiconductor. This material takes advantage of the high dielectric constant of the Titanium Oxide (TiO_2) and the large band gap of the Aluminium Oxide (Al_2O_3) which combine to form a very low leakage insulator layer with relatively high dielectric constant ($\epsilon_r = 10-12$) [43].

Indium Tin Oxide (ITO) is a well known transparent semiconductor and its properties have shown some dependence on the production method. ITO is a heavily doped n-type semiconductor with low resistivity. This material is reported to have a direct band gap with energy gap varying within the range 3-4.6 eV. The refractive index varies from 1.8 to 2.1 [44].

Aluminium + Aluminium Nitride (AlN) + Silicon (Si)

Aluminium Nitride (AlN) is a group III-V compound semiconductor. This element can be found in two structures: wurtzite and zinc blende. The structure parameters are $a = 4.37 \text{ \AA}$ for Zinc blende and $a = 3.11 \text{ \AA}$ and $c = 4.98 \text{ \AA}$ for wurtzite. Zinc blende structure is reported to be metastable. Aluminium Nitride has a band gap of 6.2 eV in wurtzite structure. This material is suitable for high-temperature electronics and optoelectronic applications. It has a relative dielectric constant of 8.6. [45]

Silicon (Si) is the most widely used semiconductor in electronic applications. This element is an intrinsic semiconductor and has a diamond crystal structure with lattice constant (a) of 5.43 \AA . The band gap is indirect and is 1.11 eV wide [42]. Silicon may be doped to convert into a p-type or n-type semiconductor. In this work, a p-type Silicon is used as the semiconductor layer of the MIS.

2.4 Thin Film Transistors (TFT)

TFTs are a special case of FETs and are composed of four main components: Gate electrode, Gate dielectric, semiconductor layer and Source/Drain contacts. All of these components may also be at the top of an isolating substrate, depending on the materials used or the applications intended.

TFT spatial arrangement may be divided into two main characteristics: the position of the gate electrode (top or bottom) and the relative position of the Drain/Source contacts to the position of the gate (staggered or coplanar). Figure 2.7 illustrates this classification. The staggered with bottom-gate configuration (b) was used for this work, which, due to its easy processing, is widely used for the fabrication of TFTs.

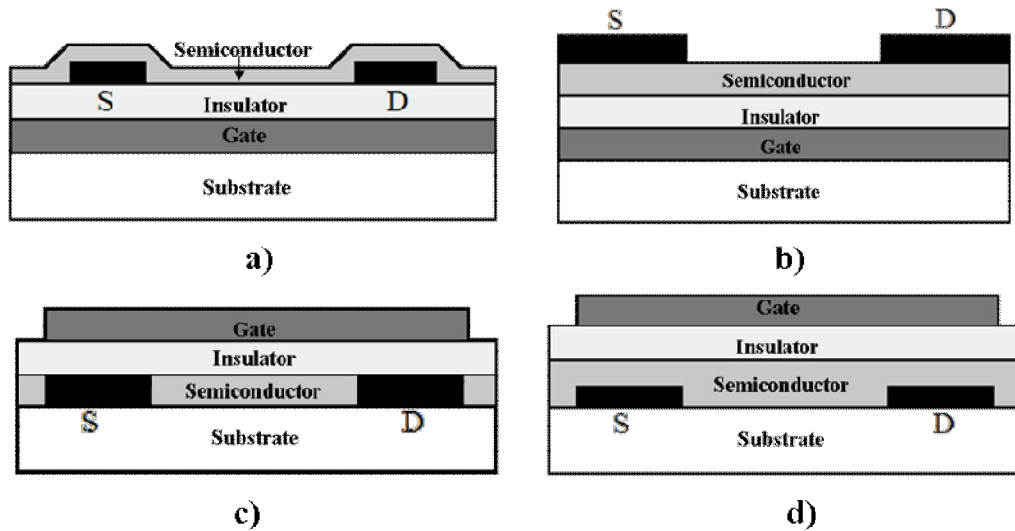


Figure 2.7 – TFT classification: a) coplanar bottom-gate, b) staggered bottom-gate, c) coplanar top-gate and d) coplanar top-gate

TFT devices may also be divided in accordance with their electrical mode of operation as the MOSFETs: enhanced-mode or depletion-mode. Enhanced-mode transistors, also called “normally off”, do not conduct current from Drain to Source when there is no Gate voltage. To switch off this kind of device you need only to stop applying voltage to the Gate. Depletion-mode devices, “normally on”, have a built-in channel at equilibrium that allows current flow even when there is no Gate voltage applied. To switch off a negative voltage must be applied to the Gate electrode. To switch on an n-type device, you either need a positive voltage if the device is an enhanced mode one, or a negative voltage if the device is a depletion mode one. An enhanced-mode transistor is usually preferred as it typically requires less energy consumption given that no energy is needed to switch it off. This is an important feature, if, for instance, it is used as a switch.

2.4.1 Mode of Operation

Field Effect Transistor (FET) is an application of the MIS behaviour. Thin Film Transistors (TFTs) are FETs and have a very similar mode operation to the MOSFETs. However, MOSFETs work in inversion mode and TFTs in accumulation mode.

The basic mode of operation is as follows: a voltage applied to the Gate electrode (V_G) induces charge movement and band bending in the semiconductor layer. This generates a variation of the conductivity in the insulator-semiconductor interface by the creation or not of a carrier channel. When voltage is applied to the Drain (V_D) contact and the Source is connected to the ground, a current flow

is generated between these two contacts (I_D). This current is thus dependent on both Gate and Drain voltages. The basic circuit to use in TFT circuits is showed in Figure 2.8.

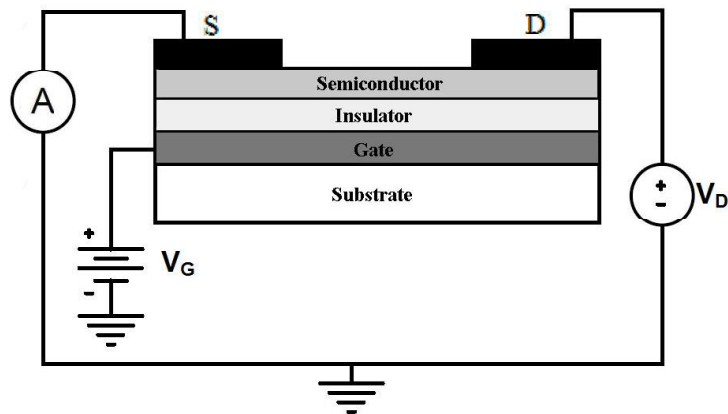


Figure 2.8 – TFT circuit configuration

The following analysis is done for an n-type TFT. Two assumptions are done: the carrier mobility and the insulator capacitance are constant along the channel length.

Off-state

When a negative is applied to the Gate electrode ($V_G < 0V$), it induces a depletion of the electrons from the semiconductor-dielectric interface, which prevents the current flow from Drain to Source when a voltage is applied to the Drain contact (V_D). A further decrease in the applied voltage simply causes a wider depletion region, which shouldn't influence the current. In this region the device is said to be off.

On-state

Linear Region

When a positive voltage ($V_G > 0V$), higher than the threshold voltage, is applied to the Gate electrode, it produces a downward band bending and an accumulation of electrons in the semiconductor-insulator interface. This creates a conducting channel between the Drain and the Source contacts that has a higher electron density than the rest of the semiconductor. When a small positive voltage is applied to the Drain contact with $V_D < V_G - V_T$, the induced electrons flow from the Source to the Drain through the channel and the current (I_D) has the opposite direction. The higher the voltage applied to the Drain, the higher the current flow.

When a Gate voltage V_G and a Drain voltage V_D are applied to the TFT, considering the conditions to achieve flat-band (Equation 2.3), the charge (Q_n) induced in the channel is:

$$Q_n(x) = -C_i(V_G - V_T - V(x)) \quad (2.4)$$

where $V(x)$ is the voltage induced in the position x of the channel, C_i is the insulator capacitance and V_T the threshold voltage. The conductance of the element dx is $\mu Q_n(x)W/dx$. The Drain current (I_D) at the position x with channel width W is thus given by:

$$I_D dx = \mu W |Q_n(x)| dV(x) \quad (2.5)$$

Integrating over the whole channel length L , we arrive to:

$$I_D = \frac{W}{L} \mu C_i [(V_G - V_T)V_D - \frac{1}{2}V_D^2] \quad (2.6)$$

On the other hand, the transconductance is given by:

$$g_m = \frac{\partial I_D}{\partial V_G} = \frac{W}{L} \mu C_i V_D \quad (2.7)$$

In this region, the TFT behaves as a variable resistance with the Gate voltage as the controlling variable. The higher are the Gate and Drain voltages, the higher is the current flow through the channel.

Saturation Region

When the Drain voltage reaches the point where there is virtually no voltage drop at the Drain end of the channel, with $V_{D sat} \approx V_G - V_T$, it prevents the channel creation. At this point, the Q_n becomes smaller and the device is said to be pinched-off. From this point on, a Drain voltage increase makes the pinch-off position move closer to the Source contact. Hence, the current flow is simply maintained by the high field and the injection of the carriers coming from the non-pinched off region. The current flow is said to be saturated.

The Drain current in saturation is given by:

$$I_{D sat} \approx \frac{1}{2} \frac{W}{L} \mu C_i [(V_G - V_T)^2] = \frac{1}{2} \frac{W}{L} \mu C_i (V_{sat})^2 \quad (2.8)$$

The transconductance in this region is given by:

$$g_{m sat} = \frac{\partial I_{D sat}}{\partial V_G} = C_i \frac{W}{L} \mu (V_G - V_T) \approx C_i \frac{W}{L} \mu V \quad (2.9)$$

Two main plots are usually obtained when analysing TFTs: output and transfer characteristic. The output characteristics are obtained by sweeping V_D for different V_G (Figure 2.9). This plot shows us how the current depends on the Drain voltage for a constant Gate voltage applied. We can thus understand, for instance, if for low V_D the TFT produces a good amplification and if it saturates for

higher Drain voltages. The transfer characteristic is achieved by sweeping V_G for a constant V_D and with this plot we are able to quantify the influence of the Gate voltage on the Drain current.

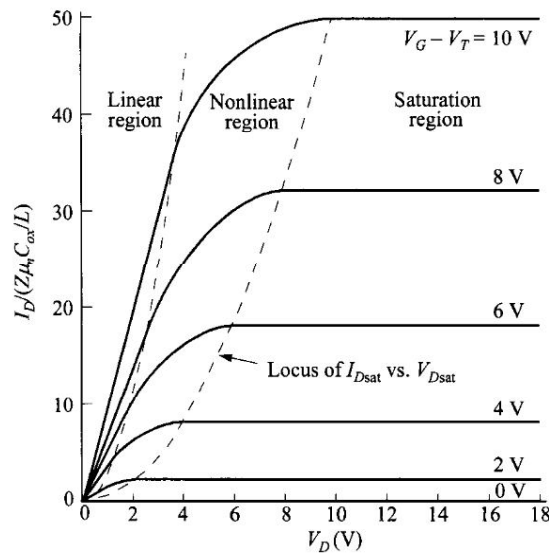


Figure 2.9 – Output characteristic of a FET [41]

2.4.2 Non-ideal TFTs

Switching on and off a TFT is simply controlled by the semiconductor resistivity variation. Since the accumulation of electrons should ideally immediately start when a Gate voltage is applied, the threshold voltage necessary to switch on the device is simply dependent of the non-ideal factors of a typical MIS structure (Sections 2.3.1 and 2.3.2).

Scattering mechanisms may seriously affect the carrier mobility in a semiconductor. These may be caused by impurities, lattice vibrations or interface/dielectric charges. The presence of traps in the semiconductor may also reduce the mobility of the carriers.

The operation of a non-ideal TFT may be significantly damaged by alternative current paths in the device such as leakage currents through the insulator. These may prevent the Drain current saturation and a true separation between the on and the off state and are not completely Gate voltage dependent. Some factors that might contribute to this behaviour are: the existence parallel conductance path between Source and Drain; internal breakdown in the semiconductor channel due to the high fields and insulator breakdown.

2.4.3 TFT Performance Evaluation

A few parameters are typically used to characterize the performance of a Thin Film Transistor such as: on/off ratio, sub-threshold swing (S) and mobility (μ).

The on/off ratio is the relationship between the minimum and maximum Drain current. A large on/off ratio is necessary to use the device as a switch.

The sub-threshold swing (S) represents the Gate voltage necessary to increase I_D by one decade. This parameter is determined by the inverse of the maximum slope of the transfer characteristic

$$S = \left(\frac{d \log(I_D)}{dV_G} \Big|_{\max} \right)^{-1} \quad (2.10)$$

The mobility (μ) represents the carrier ease to conduct through the material and may be determined in several ways, such as the transconductance in the linear region (field-effect mobility – μ_{FE}) and the transconductance in the saturation region (saturation mobility – μ_{sat}).

$$\mu_{FE} = \frac{g_m}{C_i \frac{W}{L} V_D} \quad \mu_{sat} = \frac{\left(\frac{d\sqrt{I_D}}{dV_G} \right)}{\frac{1}{2} C_i \frac{W}{L}} \quad (2.11)$$

2.4.4 TFT with ZnO, Zn₃N₂ and ZnON

ZnO

Zinc compounds have been studied as semiconductor channels by several research groups. Zinc Oxide, in particular, has been extensively used for this purpose in the past decade. This material has been mostly deposited by sputtering (~90%) on several substrates and insulators with high mobilities achieved [46]. The typical performance for an n-type ZnO device is shown in Figure 2.10.

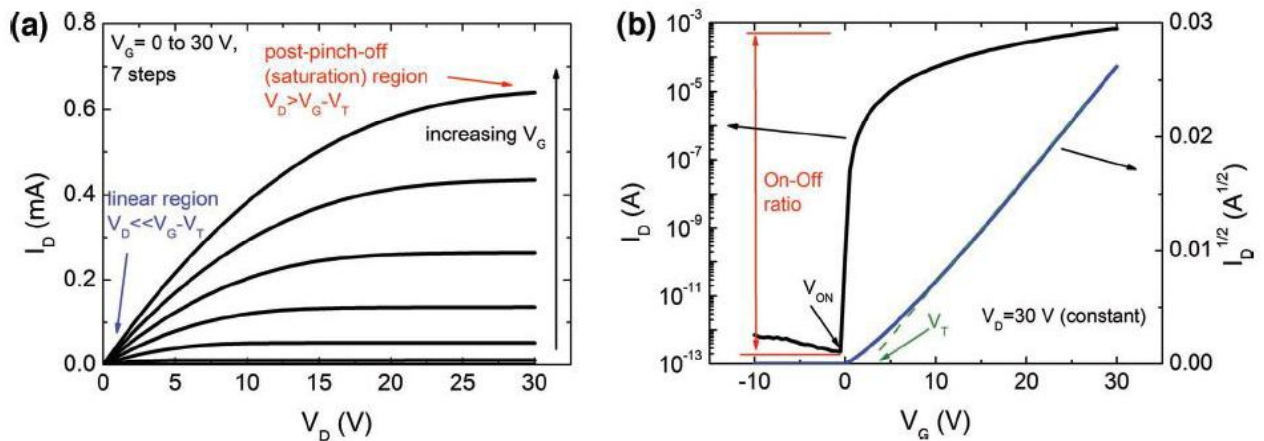


Figure 2.10 – a) Output and b) Transfer characteristics of ZnO TFTs [46]

A TFT was done by our research group (unpublished, 2010) with ZnO as channel layer deposited by PLD. A SiO₂ layer was used as the insulator. The device showed enhancement-mode behaviour, Drain-Source currents of nanoamperes and a saturation mobility of 0.11 cm²V⁻¹s⁻¹. Figure 2.11 shows its output and saturation transfer characteristics.

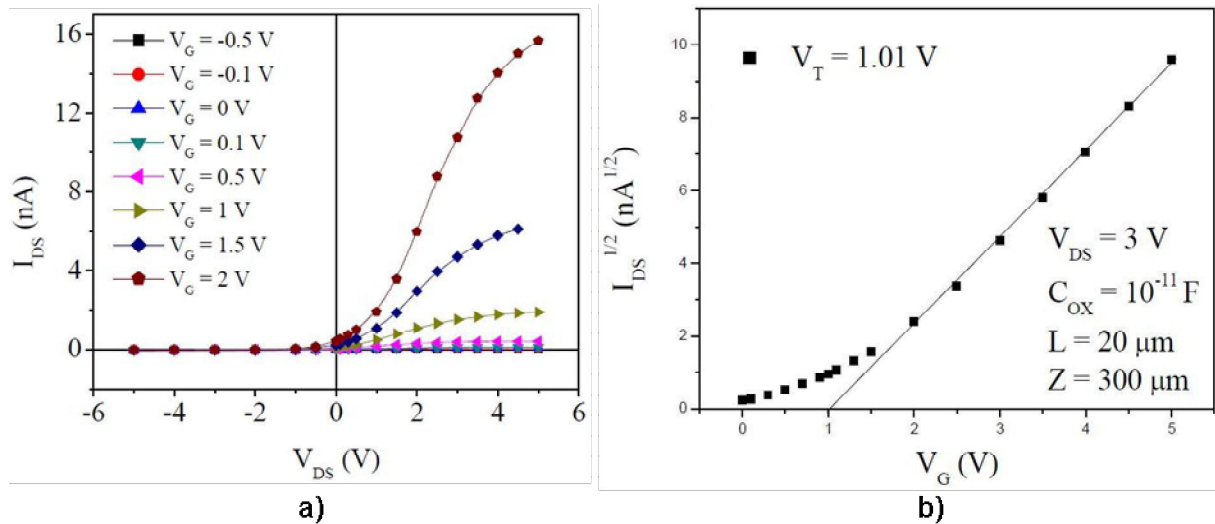


Figure 2.11 – TFT with ZnO channel layer deposited by PLD: a) output characteristic b) transfer characteristics

Zn₃N₂ and ZnON

Zinc Nitride and Zinc Oxynitride have also drawn the attention of the researchers as potential semiconductors to use as channel layer in TFTs. To our knowledge, three groups have successfully done this: two by Sputtering [30][47] and one (ours) by PLD [19]. However, further optimization is necessary as the performance is still far from the one desired for a TFT.

Concerning the PLD case [19] a Zinc Nitride layer was deposited in a staggered bottom-gate configuration. The mobility was $0.073 \text{ cm}^2 \text{ V}^{-1} \text{ s}^{-1}$ and the threshold voltage was -6.8 V making it a depletion mode device. The transfer characteristic indicated a device performance deficiency that was justified by a poor semiconductor-insulator interface and the damage done to the insulator during the deposition.

In the case of Sputtering, the reported results showed that Zinc Nitride and Zinc Oxynitride have the potential to be used as channel layer in a TFT.

For the Zinc Nitride case [30], the researchers reported that no transistor-like characteristics were observed with the as deposited structures and a rapid thermal annealing was necessary. The transistor was said to work in enhancement mode and the threshold voltage varied according to the annealing temperature: 14 V for 300°C and 6 V for 400°C . The mobility increased with increasing annealing temperature (0.02 to $4 \text{ cm}^2 \text{ V}^{-1} \text{ s}^{-1}$).

For the case of Zinc Oxynitride TFT [47], a channel width/length ratio of $40\mu\text{m}/10\mu\text{m}$ was used. The on/off ratio was said to be 4×10^8 , the threshold voltage 0.5 V, the sub-threshold 0.8 V/decade and the saturation mobility $10 \text{ cm}^2 \text{ V}^{-1} \text{ s}^{-1}$.

The comparison between these three reported TFTs is shown in Figure 2.12.

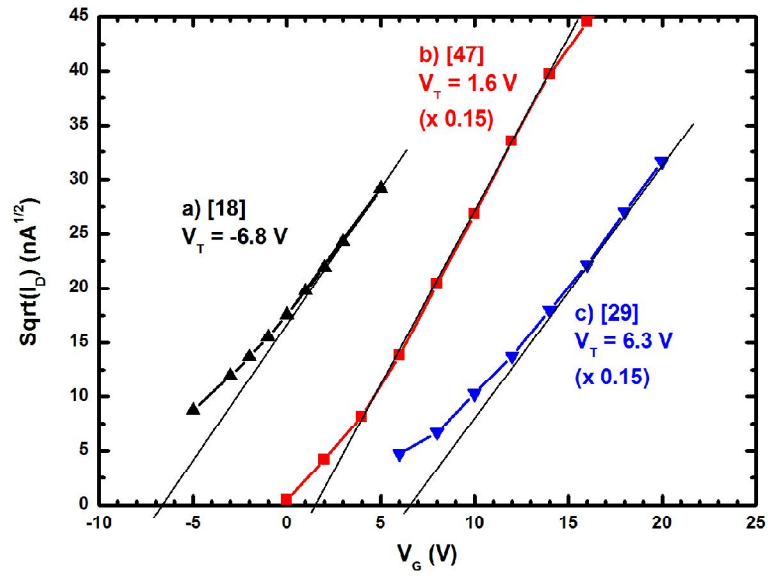


Figure 2.12 – Comparison of $\text{Zn}_3\text{N}_2/\text{ZnON}$ TFTs reported in the literature: a) [19] b) [47] c) [30]

Chapter 3

Experimental Methods

3.1 Pulsed Laser Deposition

3.1.1 Apparatus

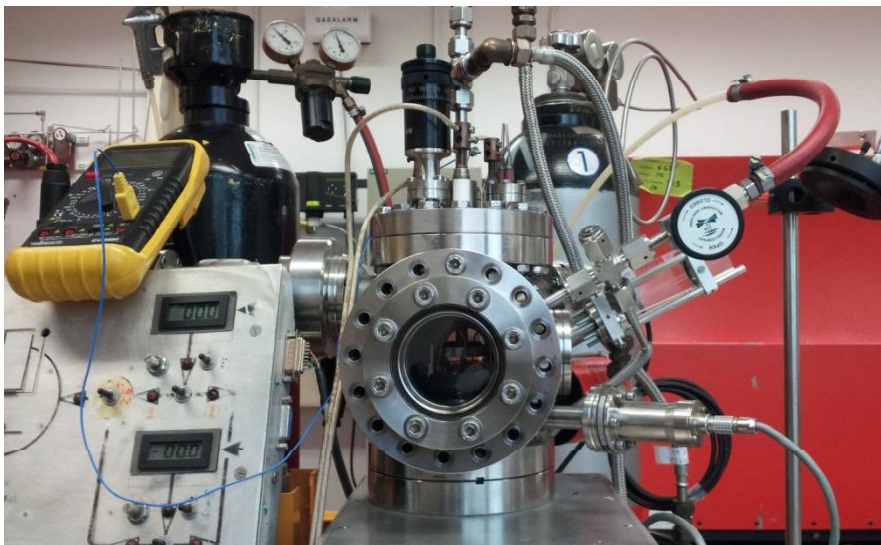


Figure 3.1 – Part of our Pulsed Laser Deposition apparatus

Our experimental apparatus has a number of instruments that makes it possible to perform the deposition. An Ultra High Vacuum (UHV) stainless steel chamber and a laser port made of quartz. A water based cooling system controls the UHV chamber temperature.

There are three different gauges to measure the pressure inside the chamber: a Pirani gauge to measure pressures from 1000 to 8×10^{-4} mbar, a cold cathode gauge to measure low pressures from 5×10^{-3} to 10^{-9} mbar and a capacitance pressure transducer to measure intermediate pressures up to 10 mbar. Two vacuum pumps create the vacuum in two steps: a rotary pump and a turbomolecular vacuum pump (Turbovac SL80). The former is turned on to reach $\sim 10^{-2}$ mbar and then the latter gets it

down to $\sim 10^{-6}$ mbar. A capacitance pressure transducer, a butterfly motor control valve and an adaptive pressure control unit were used to control Nitrogen (N_2) pressure during deposition. In our apparatus, 0.02 to 10 mbar is the range of pressures we can control. The Nitrogen pressure was set to 0.2 mbar, which is sufficient to enable the reaction of the N_2 with the ablated species, but not so high that it would prevent the diffusion of the material to the substrate.

The substrates are placed face down on a Molybdenum holder. During deposition, the substrate holder is in contact with a set of irradiating lamps that increase the substrate temperature. A variable transformer chose AC voltage applied to the heater. The substrate temperature, which could be set between RT and 600°C, was constantly monitored using a thermocouple that was connected to a multipurpose gauge. In this work we study the influence of the substrate temperature on the film quality.

A Zinc metallic target (99.9999% purity) from Alfa Aesar was used as target. The target was polished to obtain a uniform surface. As the laser beam forms cavities as it hits the target surface, the laser position was changed regularly during deposition. The target was placed at the bottom of the chamber cavity and the distance between the sample holder and the target was set to 3 cm.

For this work a Nd:YAG laser was used in the Q-switching mode. The pumping system is composed by two flash lamps. The fundamental wavelength of the Nd:YAG amplifier is 1064 nm. Two crystals are used to generate, by second and fourth harmonic generation, two other wavelengths. Hence, we have available three wavelength lines: 266 nm (Ultraviolet line - UV), 532 nm (Green line) and 1064 nm (Infrared line - IR). In this work we tested different wavelengths to see which wavelength is more suitable for the deposition of Zinc Nitride films. The laser has an auxiliary water based cooling system to control the temperature. The maximum pulse energy is 200mJ. The frequency and duration of the pulses were set to 10 Hz and 5 ns in this work. The laser pulse hits the target with a 45° angle of incidence.

3.1.2 Experimental Procedure

The experimental procedure used has three main stages: preparation, deposition and shut down.

In the preparation stage, the substrate is placed on the sample holder and, after being polished, the target is placed in the chamber cavity. The chamber is then closed and the rotary and turbo vacuum pumps are turned on. A 24 hours waiting period is done so as to achieve an adequate base pressure.

In the deposition stage, after opening the cooling water and the ventilator, the heater is turned on slowly. The adaptive pressure control unit is used to set the Nitrogen pressure. The laser is then turned on and properly focused. When the chosen substrate temperature is achieved, the deposition starts. During this process, the laser hitting point is changed every five minutes.

In the shut down stage, the laser and the heater are turned off. The sample is allowed cooled down in Nitrogen background. Both vacuum pumps are then turned off and the sample is taken out of its holder.

The following sections were written using [41], [42] and [48] as references, which may be consulted for further information.

3.2 Thermal vaporization

The production of high quality metal contacts is a fundamental factor in this experimental work. Aluminium was used as it has been proven that this metal forms ohmic contacts with Zinc Nitride samples [27] and it is an economical choice.

Metallization was achieved using a physical vapour deposition method called thermal vaporization. High vacuum ($\sim 10^{-5}$ mbar) is used to avoid contamination from environmental elements. A high quality Aluminium piece is placed in a tungsten basket at the bottom of the deposition chamber. The samples and their masks are placed on the proper holder at the top of the machine and the chamber is closed. After a sufficiently low pressure has been achieved, the metallization may start. The tungsten filament, which has a high melting point ($\sim 3000^{\circ}\text{C}$), is connected to a low voltage, but high current, power supply. The heat is transferred to the Aluminium piece, which has a lower melting point, causing its vaporization. The aluminium vapour rises in the machine until it hits the samples where it solidifies again creating the desired metallic contacts. The instrument used was Edwards Coating System 306A.

3.3 I-V Measurements

3.3.1 Instrumentation

Two instruments were required to measure Current-Voltage (I-V): a voltage source and a picoammeter. A DC Voltage is applied to the device under test (DUT) and the correspondent current was measured by the picoammeter. The corresponding circuit is presented in Figure 3.2.

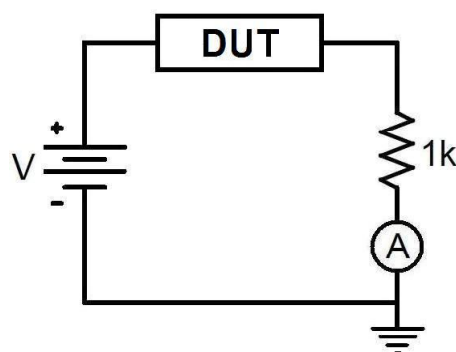


Figure 3.2 - I-V measurements circuit

A Lock-In Amplifier SR830 was used as DC Voltage Source. Its Auxiliary Outputs are available on the rear panel.

resistance between the output of the sample and the input of the picoammeter was used to protect the instrument from unexpected current peaks. This picoammeter features a “Zero Correct” function that

subtracts from the measurements read by the instrument the current that exists even when there is no voltage applied to the system.

The RS232-GPIB interface connects the PC to the two instruments. The interface is a National Instrument GPIB-232CT-A, which allows communication with up to 14 instruments at the same time. The interface was connected to the PC by a Serial Cable RS232 and to both instruments by two GPIB cables, as shown in Figure 3.3. Several switches on the interface allow us to control the serial communication in accordance to needs.

For every communication with either instrument the user has to send these commands to the interface:

- WRT X – write on the instrument with the address X
- Command – command intended for the instrument with address X
- RD #Y X – read Y bytes from the instrument with the address X

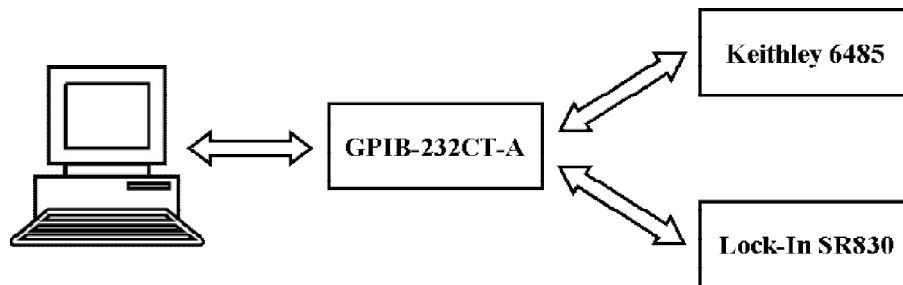


Figure 3.3 – PC-Instruments communication with the interface

3.3.2 Program

A program was developed on purpose for this work to ease measurement workload and save time. It basically records instruments data. We have designed the program on a Labview 8.6 software structure.

The user must define several settings on the Labview front panel as per these three groups:

- Communications: serial port, baud rate, parity, Keithley and Lock-In GPIB addresses;
- Zero check: zero check range;
- Measurements: measurement range, Vmin and Vmax, dV, AuxOut, maximum current allowed, VG, hysteresis and so on.

It is recommended to evaluate manually the sample behaviour before choosing the zero check and measurement parameters. After this, the user can choose to make a Zero Check or a measurement and run the program. At the beginning of the measurements and every time the measurement circuit suffers any changes, a Zero Check is required.

Zero Check

A picoammeter Zero Check within the range decided by the user is carried out. The front panel display the information that Zero Check was done.

Measurement

Lock-In does a voltage sweep, with step dV . The corresponding current is measured. The voltage sweep is done with or without hysteresis:

Without hysteresis - $V_{min} \rightarrow V_{max}$.

- With hysteresis - $0 \rightarrow V_{min}$, $V_{min} \rightarrow V_{max}$, $V_{max} \rightarrow V_{min}$ and $V_{min} \rightarrow 0$.

VG

A steady-state DC voltage output is supplied to a third point of the sample to carry out, for instance, a $I_{DS} (V_D)$ analysis with V_G constant.

Stop

The program is abruptly stopped either if the user presses the STOP button or if the current reaches the maximum allowed value that was formerly defined by the user.

Data display and storage

The voltage/current pairs are displayed numerically and graphically on the front panel, voltage along the x axis, current along the y axis (I-V curve), and both stored in an ASCII file. The data are constantly stored; hence even if the measurement is abruptly stopped, the data acquired until then are still saved.

Resistivity determination

If there is an ohmic behaviour, obtaining its resistivity (ρ) is straight forward: just take the I-V curve inverse slope and obtain resistance (R). Knowing the film (t) thickness, the metallic contacts width (w) and the distance between them (l), resistivity is calculated by inverting Equation 3.1.

$$R = \rho \frac{l}{wt} \quad (3.1)$$

3.4 Transmission

When the light hits a sample, it is either reflected, absorbed or transmitted. If a photon has less energy than the band gap of the material ($h\nu < E_{gap}$), it has not enough energy to excite electrons from the valence band to the conduction band and thus be absorbed. So, it is transmitted through the film or is reflected according to the refractive index value. If a photon has more energy than the band gap ($h\nu > E_{gap}$), it can be absorbed by the material and cause the creation of an electron-hole pair. The energy band gap is thus the threshold energy for absorption to occur and may be quantified by studying the optical absorption of a material. This absorption is characterized by the absorption absorbed.

Transmittance is the fraction of incident light at a determined wavelength/energy that passes through a material. The transmittance of the material each wavelength/energy is expressed by the Beer's law.

$$T = (1 - R^2) e^{-\alpha d} \quad (3.2)$$

where T is the transmittance, R the reflectance, α the absorption coefficient and d the material thickness. In most of our measurements, the film reflectance was negligible and it will not be taken into account in the analysis. Hence, knowing the transmittance, the absorption coefficient is simply computed by inverting Equation 3.2.

The method introduced by Tauc *et al.* [49] was used to determine the material optical band gap. This method is based on the assumption that the absorption coefficient is a parabolic function of the incident energy defined by:

$$\alpha \propto \frac{(h\nu - E_{gap})^m}{h\nu} \quad (3.3)$$

where $h\nu$ is the photon energy and m is a coefficient dependent on the transition between the bands. If it is a direct transition, m is equal to $\frac{1}{2}$ and if it is an indirect transition m is equal to 2. Hence, plotting $(\alpha h\nu)^2$ versus the incident photon energy and taking the interception of the linear part of the plot with the energy axis shows the direct optical energy band gap E_{gap} . The same procedure is applied to the $\alpha h\nu$ versus the photon energy. The experimental setup shown below in Figure 3.4 was used.

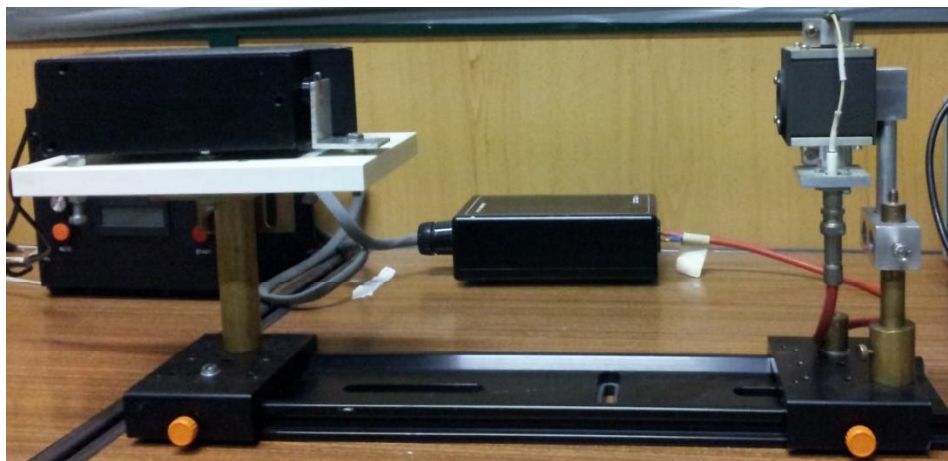


Figure 3.4 - Experimental setup for the optical measurements

To start off with, the lamp spectrum is measured and only afterwards is the sample analysed. The light coming from the lamp hits the sample and those photons that pass through it are collected by the spectrometer. A diffractometer separates the photons by wavelength and directs them into different cells of the CCD detector that counts them. The spectrometer is connected to the PC and an Intensity

vs Wavelength plot is shown on the screen. These data can be saved as an ASCII file to be used in further analysis.

The lamp is a Xenon lamp with a power of 75 W. The lamp spectrum is shown in Figure 3.5.

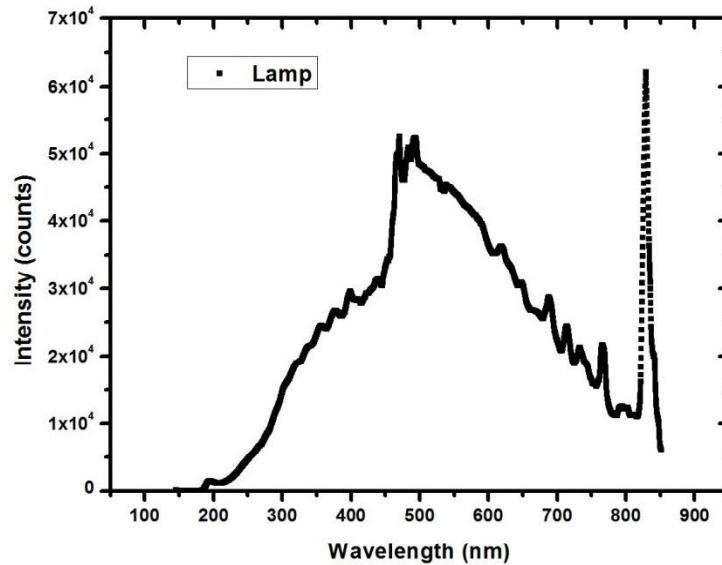


Figure 3.5 - Xenon lamp spectrum

In Figure 3.5 shows that the lamp has a wide spectrum but its emission is not uniform, having peaks in the visible region. We have used an Horiba Jobin Yobin VS140 Linear Array Spectrometer that has a range of wavelengths 150 nm to 850 nm. However, from our experience, the data it provides should not be taken into account for wavelengths outside the range [200-800 nm]. The software LynearApp, provided with the spectrometer, was used to acquire the data.

3.5 C-V Measurements

C-V measurements are commonly used to evaluate MIS structures. There are several methods to make these measurements, using more or less complex technology. In this work, we used a simple circuit taking into account the known electric behaviour of two capacitors in series.

In the circuit used, two devices are put in series: a commercial capacitor, as reference capacitance, and the device under test (DUT). The circuit is shown in Figure 3.6. An AC signal (V_m) with defined amplitude is applied to point A. A capacitive voltage divider thus exists between the point A and the ground. Knowing the applied AC voltage, the reference capacitance and the voltage drop between the point A and B the DUT capacitance may be determined by Equation 3.4.

$$C_{DUT} = \frac{C_{Ref} \cdot V_{AB}}{V_m - V_{AB}} \quad (3.4)$$

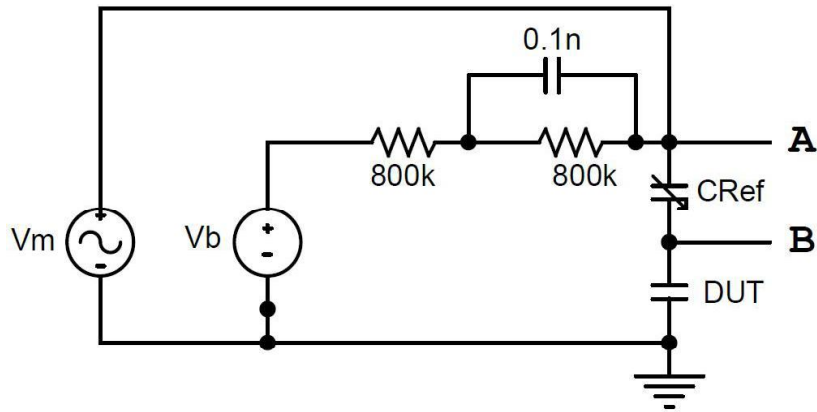


Figure 3.6 - C-V measurements circuit

A bias voltage (V_b) is also applied to both the devices. As explained in Section 2.3.1, the capacitance of an MIS structure varies depending on the region of operation the device is on and on the AC signal frequency. From the Capacitance-versus-Voltage curve, we are able to obtain a set of information about the DUT. Among others it can be determined the doping of the semiconductor and the thickness of the insulator.

A program built on Labview 8.6 was used to control both the applied voltages and to acquire the voltage V_{AB} necessary to determine the DUT capacitance. The AC signal frequency and amplitude, the range, step and speed of the bias voltage sweep are defined by the user according to the needs. The V_b/V_{AB} pairs are displayed numerically and graphically on the front panel and both stored in an ASCII file. V_{AB} is then converted into the capacitance using the Equation 3.4.

The auxiliary RC circuit is used to avoid any current peaks that may occur in the circuit.

3.6 Scanning Electron Microscopy (SEM)

A Scanning Electron Microscope (SEM) is a high-resolution microscope that uses a focused electron beam to scan the sample. This method is non destructive and is used to analyse the topology, texture, chemical composition and crystalline structure of the material. It is especially advantageous because electrons may have a extremely short wavelength, depending on the energy with the De Broglie relation, and have a larger penetration length than photons.

A SEM is a complex instrument made up of a number of components. An electron gun generates the electrons that are then accelerated and pass through a set of condenser lens that focus the beam and direct it to the desired position. Using the scanning coils, which deflect the electrons in the x and y axis, the electron beam changes its incident position over time and traces through the area of the sample desired, enabling us to have a complete image of that area. The information coming from each position of the electron beam is displayed to the correspondent pixel on the PC screen; hence the image displayed has a perfect spatial correspondence to the sample structure.

When the electron beam interacts with the surface of the sample, secondary electrons are dislodged and collected by the detector. The brightness of the image originated is mainly dependent on the number of secondary electrons detected. The interaction of the high energy electrons with the

material surface can also cause the emission of different signals: back-scattered electrons (BSE), diffracted backscattered electrons (EBSD), characteristic X-rays, visible light (cathodoluminescence), transmitted electrons and heat. These signals may also be obtained and analysed together with the secondary electrons in order to have more complete information about the sample.

The magnification is simply obtained by the relationship between the dimension of the scanned area and the display dimension. Considering that the display size is usually constant, a higher magnification is obtained by decreasing the area scanned. The magnification is therefore controlled by the power supplied to the scanning coils and not by the lenses.

A FEG-SEM JEOL 7001F with Oxford light elements EDS detector and EBSD detector, from ICEMS' MicroLab was used in this experimental work. It allows a magnification up to 100,000 times. In this dissertation, we will pay special attention to the 1,000x and 50,000x magnified images.

A previous sample preparation may be needed in some cases, depending on the sample. As the image is scanned by electrons, the sample must be conductive; hence, if that is not the case, one must cover it with a thin layer of a conductive material. In this work, a Polaron sputter coater was used to deposit a layer of Cr.

3.7 X-Ray Diffraction (XRD)

X-Ray Diffraction is a non destructive method to determine the structure and crystallinity of a material. The basic principle behind this method is that as an electromagnetic wave hits a crystal structure, it is reflected partially by each parallel plane of atoms in the crystal. It is assumed that the scattering is elastic and the X-ray loses no energy in the process. It is also assumed that each plane does not reflect completely the wave; otherwise the X-ray would only be able to reach the first array of atoms in the sample. The diffracted waves interfere positively or negatively forming a diffraction pattern with several maxima and minima of intensity that can be recorded as a pattern. The pattern provides a large body of information about the material. The position of the m maximum, assuming that the refraction index is unitary, can be described by the Bragg relation:

$$m\lambda = 2d \sin \theta \quad (3.5)$$

where m represents the order of the maximum, λ the wavelength, d the distance between planes of atoms and θ the X-ray angle of incidence. The X-rays are used as electromagnetic waves because their wavelength is of the order of magnitude of the distance between atoms in a crystal, which is usually a few Angstroms. X-Ray diffraction at a crystal structure is shown in Figure 3.7

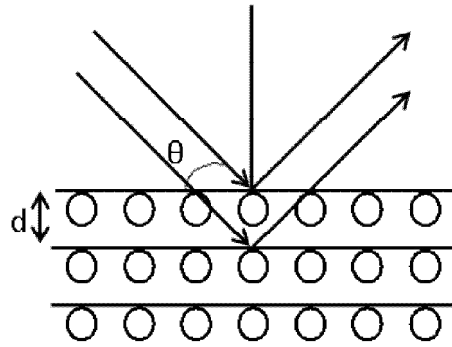


Figure 3.7 – X-Ray diffraction on a crystal structure

The planes of atoms in a crystal are represented by a set of three integers called Miller indices. These can be obtained by determining the integer intercepts of the plane with the crystal axes, take the reciprocals and reduce these to the smallest set of integers h , k and l that represent the Miller indexes. The plane in question is then named (hkl) . The distance between (hkl) planes is determined by the crystal structure and substituted directly in the Bragg relation to determine the angle correspondent to a maximum. Hence, there is a correlation between the planes of the crystal, the incident angle of the X-rays and the maxima in the X-ray diffraction pattern. This is very helpful to determine the crystal structure of a sample.

The crystallite size (D) may be calculated using:

$$D = \frac{0.9\lambda}{B \cos\theta} \quad (3.6)$$

where B FWHM the full width at half maximum, λ the X-ray wavelength and θ the diffraction angle.

In a XRD instrument there are three main components: X-ray tube, sample holder and X-ray detector. The X-rays are emitted applying a high voltage to a filament, causing the emission of X-rays the energy of which is determined by the filament material. The angle of incidence is determined by the position of this tube. The sample is placed on a rotating sample holder to be able to measure a larger area of the sample. The detector has also to change its position to be able to capture the diffracted X-rays. The results of these measurements are usually presented in a 2D plot with 2θ in the x axes and the number of counts in the y axes.

The XRD instrument used is a Philips Pw3020 with $\text{CuK}\alpha$ radiation ($\lambda=1.54\text{\AA}$).

3.8 X-Ray Photoelectron Spectroscopy (XPS)

X-Ray Photoelectron Spectroscopy (XPS) is a non-destructive technique to identify the chemical composition of the material surface and its physical principle is based on the photoelectric effect.

A monochromatic X-Ray hits a surface with a defined and well known energy. If its energy is higher than the electron binding energy, the electron is ejected off the material and can be detected by the instrument. The relation between the electron binding energy (E_b) and its kinetic energy detected in the spectrometer (E_s) is the following:

$$E_b = E_{XR} - E_s - e\phi_s \quad (3.7)$$

where E_{XR} is the energy of the incident X-rays and E_s is the spectrometer work function. As the sample and the spectrometer are in contact, their Fermi levels are forced to line up.

The binding energy of an electron depends on the atomic environment. Hence, it is influenced by the element atomic number and can be used to determine the chemical composition of the material. For this, one must use standard data available in several sources.

Despite the fact that X-rays have a good penetration in materials XPS is a surface characterization technique because only electrons from the upper part of the sample (~10nm) are able to escape and be detected by the instrument. If an electron is emitted in a lower layer of the material, it is easily trapped or recaptured by its surroundings. To analyse a deeper layer of the sample, it can be sputtered shortly before the XPS analysis. However, this procedure has the disadvantage of partially destroying the sample in the process.

The XPS device is composed of three fundamental instruments: a high vacuum pump, an X-ray emission source and a spectrometer. The measurements are taken at high vacuum to avoid environmental contamination and interaction between resulting electrons with the air molecules. X-rays are generated in the same way as in XRD in a cathodic tube. The electrons are detected by a spectrometer that can count and separate the electrons by their energy. The XPS data is usually displayed in a 2D plot with the binding energy along the x axis and the intensity along the y axis. The intensity of the peaks is proportional to the number of electrons detected for each energy level.

XPS measurements were performed on a VSW XPS system with the Class 100 energy analyzer.

Chapter 4

Results on Zn₃N₂ Film Deposition

In Chapter 2 we described previously reported problems with the production of Zinc Nitride thin films. Different production methods seem to produce different results. The deposition of Zinc Nitride thin films by PLD is still poorly studied and the ideal conditions for this method are yet to be determined. In this Chapter, we study the influence of two important parameters of PLD on film properties: the laser wavelength and the substrate temperature. To start off, the influence of the laser wavelength was studied by varying only this factor and later on we looked at the influence of the substrate temperature.

In this process, thin films were deposited on a Glass (BK7) substrate which is an insulator and transparent to visible light ($E_{\text{gap}} \sim 4 \text{ eV}$) thus allowing optical measurements. The experimental procedure for the deposition followed the steps stated in Section 3.1.2.

Figure 4.1 shows the plasma plume during a Zinc Nitride deposition. The emission of a purple light that we observe is characteristic of Nitrogen plasma.

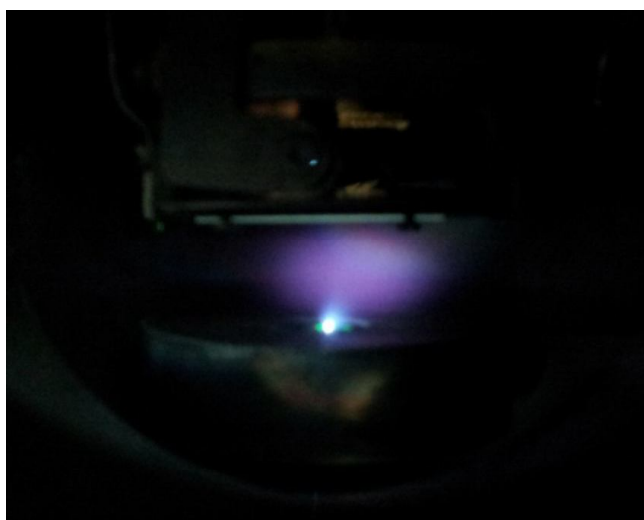


Figure 4.1 - Plasma plume during a Zinc Nitride deposition

4.1 Film Properties versus Laser Wavelength

One of the fundamental parameters in PLD is the laser wavelength. Since our instrument has three possible wavelength lines, in this step we studied the most suitable one for the deposition of Zinc Nitride thin films. Table 4.1 shows the main deposition parameters of the three analysed samples.

Sample	Deposition Duration	Laser Wavelength
	hours	nm
ZnN23	2	266
ZnN21	2	532
ZnN22	1	1064

Table 4.1 – Laser wavelength and deposition duration each sample

4.1.1 Morphology

Figure 4.2 shows the morphology comparison of the films deposited with the three lines of the laser. To obtain these images the magnification of the SEM microscope was set to a micrometric scale.

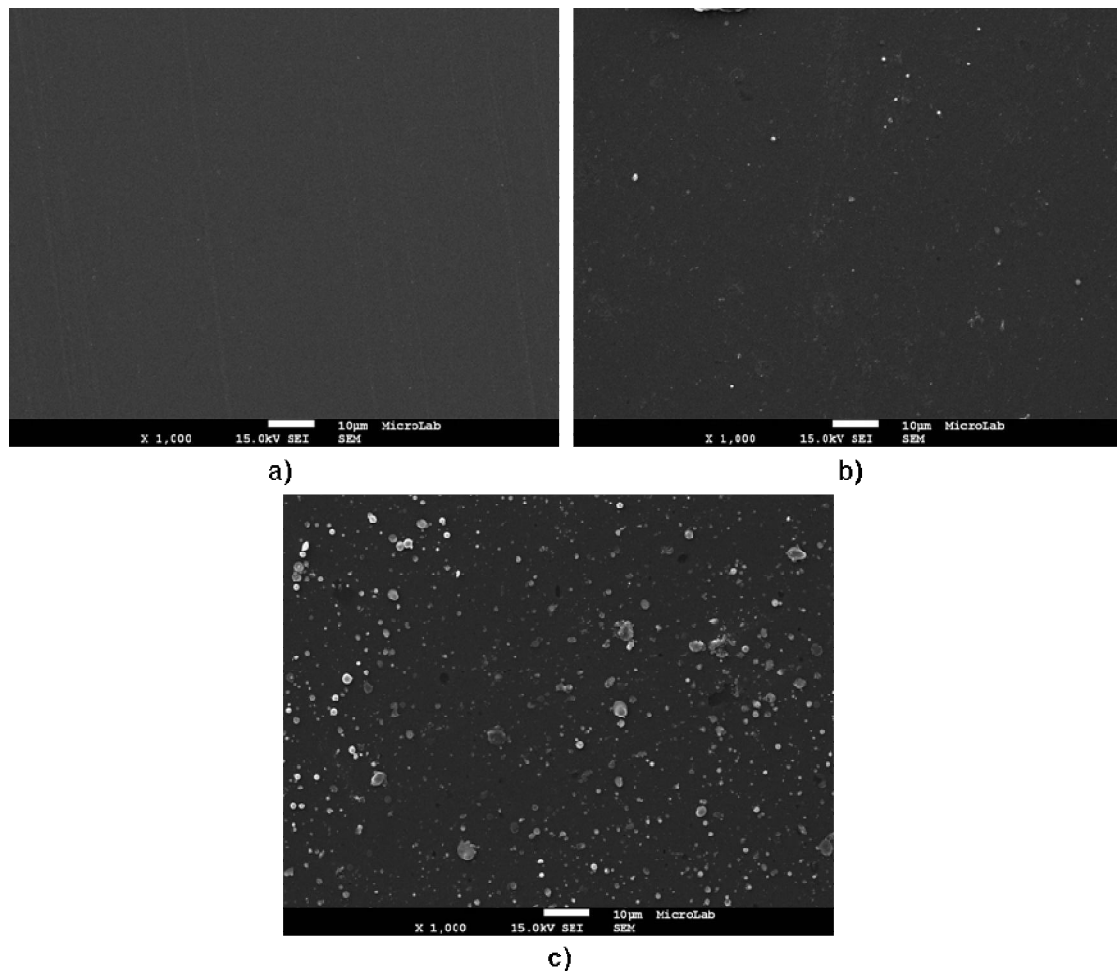


Figure 4.2 - SEM images with 1000x magnification for different laser wavelengths: a) 266 nm, b) 532 nm and c) 1064 nm.

As predicted in Section 2.1.2, the films produced by PLD have particles at the surface. These particles have a micrometric size and, taking into consideration their size and geometry, were probably ejected from the target (particulates). The fact that we used a metallic target promotes the deposition of these unwanted particulates. Since the substrate is heated to 400°C, the particles are melted and gain this splashing geometry. We also found that the films have pinholes. These structures are due to the unintentional sputtering caused by the fraction of the particles that hit the film with high kinetic energy and are unable to deposit in it, as reported by the literature.

The particles were particularly detected when using the infrared line (ZnN22). Their presence in the films increases with increasing wavelength, just as it is predicted by the literature presented in Section 2.1.2 [8].

In Figure 4.3 the microscopy of the three samples was done in the nanometric scale allowing a better understanding of the film morphology. The films are uniform and have different grain sizes, with larger dimensions for the films deposited with the green line. At this wavelength, the grain size appears to be 40-50 nm.

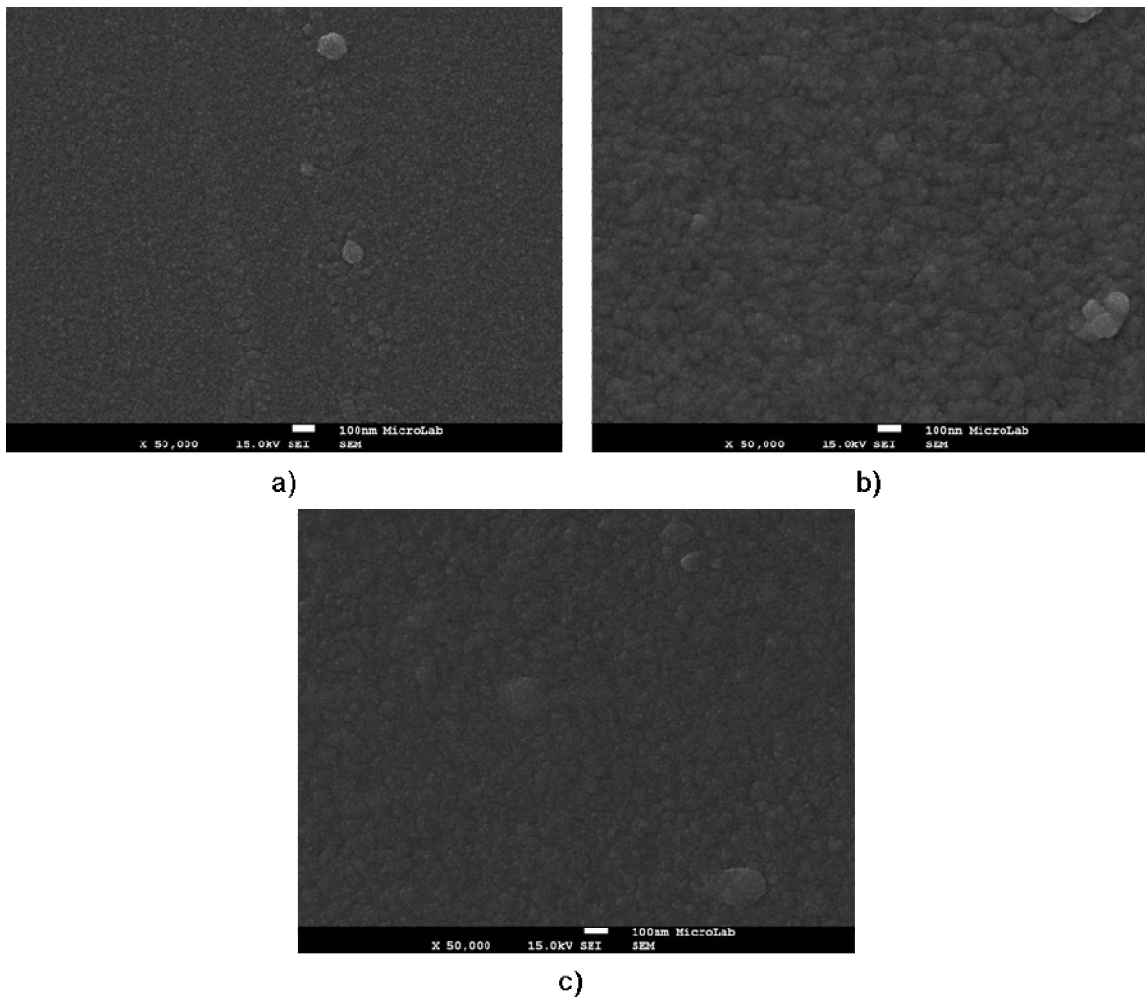


Figure 4.3 - SEM images with 50,000x magnification for different laser wavelengths: a) 266 nm, b) 532 nm and c) 1064 nm.

Concerning the morphology, the UV line seems to produce the films with the best quality seeing that there are fewer particles and larger grain sizes on these films. However, it was also noticed that this line had a very low deposition rate and sometimes even no film was deposited at all. We later on realized that during the deposition the plume intensity diminished. This was confirmed by analysing the transmission of the chamber window. The transmittance of the window was re-established after cleaning with ethanol and Hydrofluoric Acid (HF) as shown in Figure 4.4.

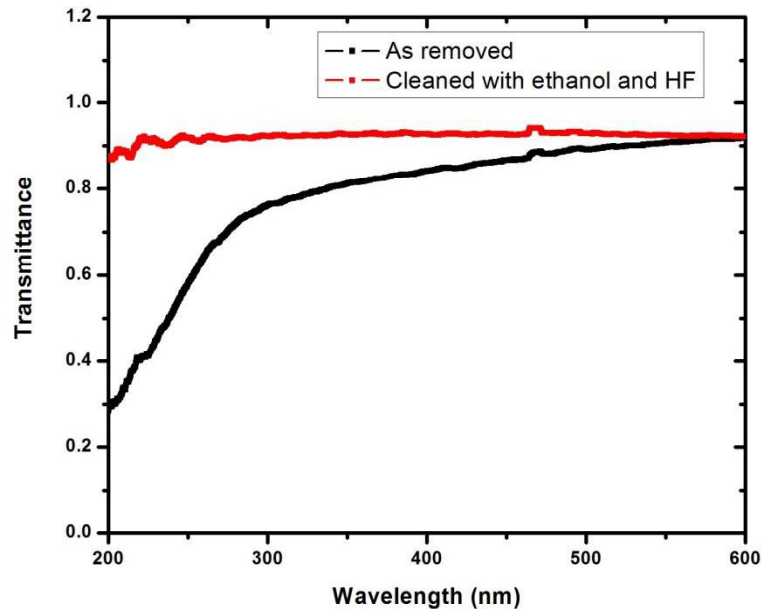


Figure 4.4 – Quartz window Transmittance spectrum as removed and cleaned with ethanol and HF

We can observe in Figure 4.4 that the transmittance of the window significantly changed after being cleaned with ethanol and HF. This variation may be explained by the fact that during the deposition, particularly at high temperatures, a Zinc compound travels through the chamber and when in contact with the walls and windows, which are at a lower temperature, solidify and deposit on them. Consequently, as time goes by, a layer of a Zinc compound with low band gap is formed all over the chamber affecting the transmission of the quartz window and diminishing the power of the pulse that hits the target. The transmittance of the as removed window at the wavelength of 266 nm (UV) is approximately 67% and 90% at 532 nm (Green). Therefore, the power diminishing effect is particularly significant for lower wavelengths. This observation combined with the fact that the UV line has originally a lower power may explain the extremely low deposition rate of the UV line. The wavelength of the Infrared line is outside our spectrometer range and its transmittance could not be determined.

4.1.2 Optical Properties

With the purpose of having a better understanding of how the optical film properties depend on the laser wavelength, transmittance measurements were performed.

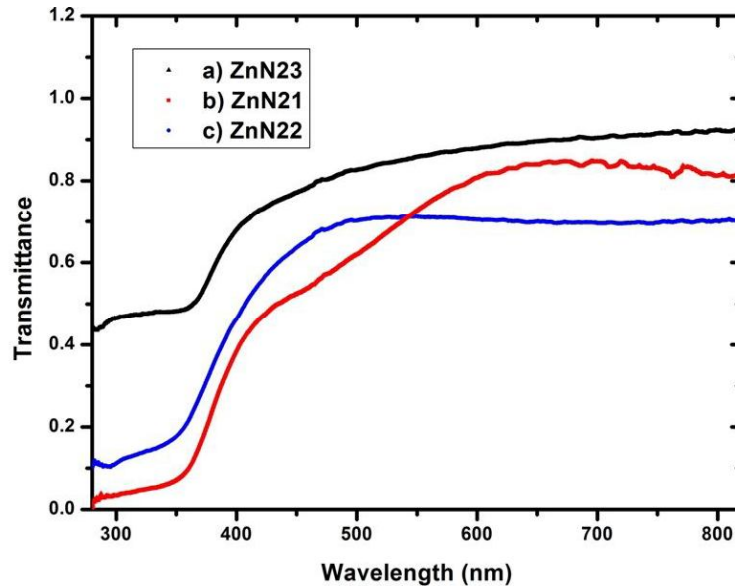


Figure 4.5 – Transmittance spectrum for different laser wavelengths: a) 266 nm, b) 532 nm and c) 1064 nm.

Figure 4.5 presents the transmittance of the three samples. At low incident photon wavelengths, even beyond the optical band gap, there is light transmission leading to a pedestal. This behaviour may be explained by the non uniformity of the films, the film thickness and the presence of pinholes shown in the SEM images. The pedestal height has its maximum for the sample ZnN23 (UV) and its minimum for the sample ZnN21 (Green). In sample ZnN21 one might detect an interference fringe pattern that can be explained by the multiple reflections at the different interfaces (air-film-substrate) that take place for films with a larger thickness.

4.1.3 Electrical Properties

After depositing Aluminium contacts on the samples, Current-Voltage measurements were undertaken to show the influence of the wavelength in the electrical properties of the films. The film resistivity was then computed taking the geometrical parameters into account and using Equation 3.1.

Figure 4.6 shows typical I-V characteristics for each of the samples mentioned above. It is clear that the films have an ohmic conduction. To calculate their resistivity we used the method described in Section 3.3.2 and the results are stated in Table 4.2.

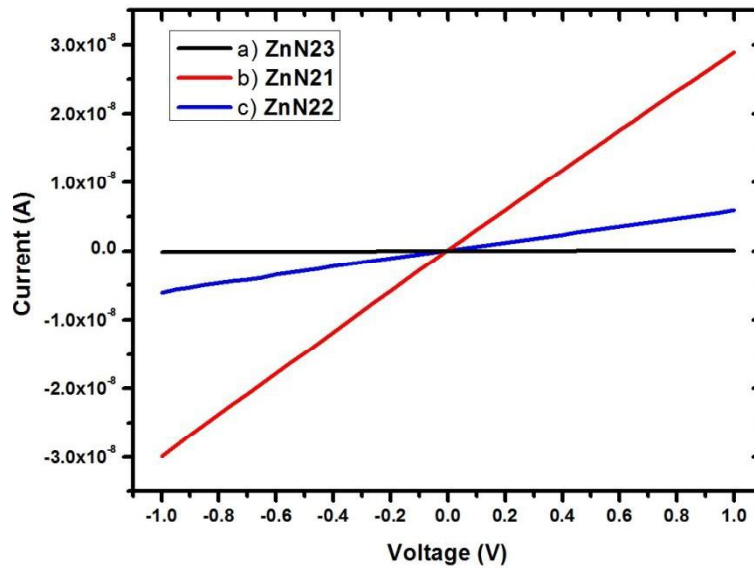


Figure 4.6 – I-V curves for different laser wavelengths: a) 266 nm, b) 532 nm and c) 1064 nm.

Sample	Laser Wavelength	Resistivity
	nm	Ω .cm
ZnN23	266	3760
ZnN21	532	72
ZnN22	1064	338

Table 4.2 – Resistivity for different laser wavelengths

The resistivity significantly varies with the laser wavelength, within orders of magnitude, and has its minimum with the Green laser line. This phenomenon may be explained by the different morphologies shown above. We can also observe that the maximum of conductivity corresponds to the maximum of grain size in the Green line deposition. Moreover, the existence of pinholes, particularly present in the IR deposited sample, and the film thickness, lower in the UV deposited sample, also deeply affect the current flow.

4.1.4 Conclusion

After analysing the previously stated results and weighting the advantages and disadvantages for the use of each wavelength, we decided to use the Green line. This is a compromise solution since this line reaches the target with an intermediate power. This power is enough to have a reasonable deposition rate (higher than the UV line) and to avoid excessive damage of the target and an extreme deposition of particles (as the IR line). Also, the optical and electrical properties seem to be the most adequate for our purposes.

From this point on, all the depositions presented were done using this line (532 nm).

4.2 Film Properties versus Substrate Temperature

In this step, the influence of the substrate temperature on the film properties was studied. For this purpose, a different temperature was chosen for each sample deposition, taking the following values: 100°C, 200°C, 300°C, 350°C, 400°C and 500°C. The samples used to undertake this study and their substrate temperatures during deposition are displayed in Table 4.3.

Sample	Substrate Temperature
	°C
ZnN32	100
ZnN33	200
ZnN34	300
ZnN39	350
ZnN35	400
ZnN37	500

Table 4.3 – Substrate temperature during deposition of each sample

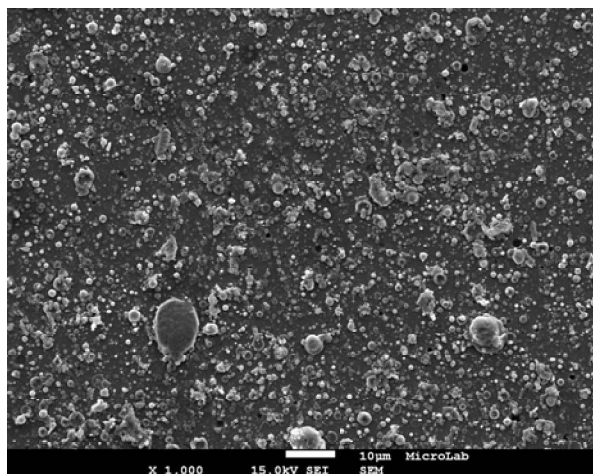
4.2.1 Morphology

In Figure 4.7 we display the SEM images of each sample at micrometric scale. The film uniformity and particle presence is extremely dependent on the substrate temperature. Considering their micrometric size and rounded shape, we can infer that these are particulates originated during the laser-target interaction phase of the PLD. At low temperatures, there is a higher density of those.

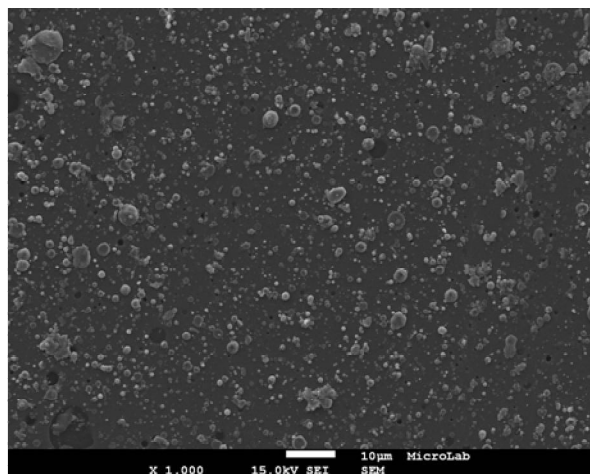
The particulates travel through the space between the substrate and the target, which is filled with Nitrogen, and their surface suffers nitridation forming Zn-N bonds. However, the inside is mainly composed of metallic Zinc. As the deposition temperature rises, it causes the particle melting which also happens in Nitrogen background inducing their nitridation.

In addition, the particles that reach the substrate with high kinetic energy might cause the unintentional sputtering and pinholes at the film surface. This effect is also diminished with a higher surface temperature since the film structure is able to reorganize itself and fill some of the pinholes created.

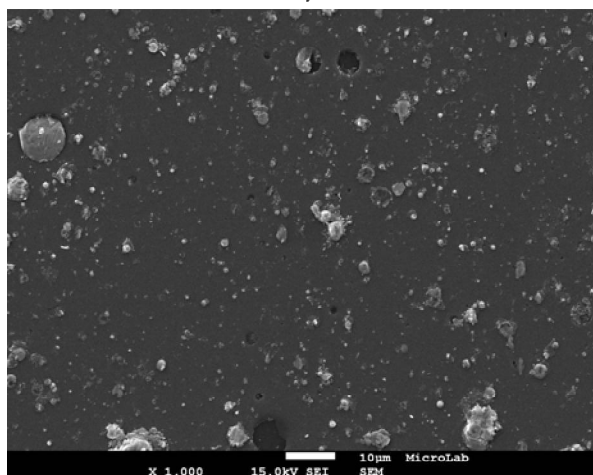
The particle presence dependence on temperature presented is in accordance with the typical results reported by the literature when using PLD as production method.



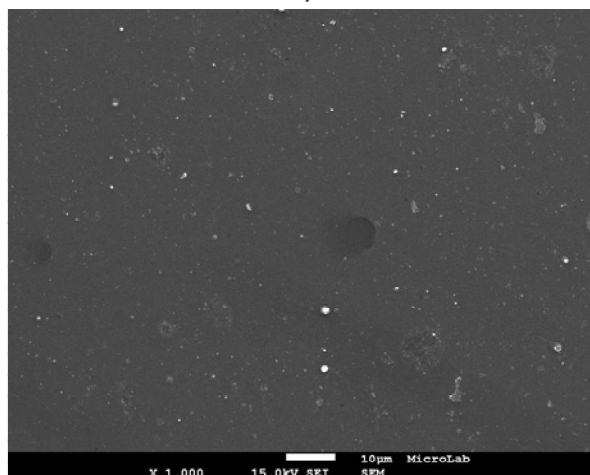
a)



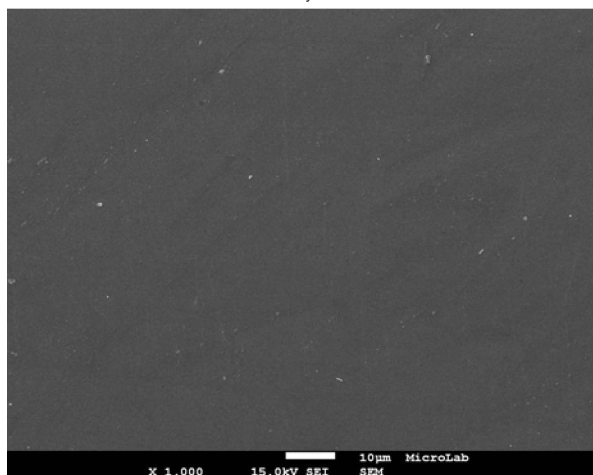
b)



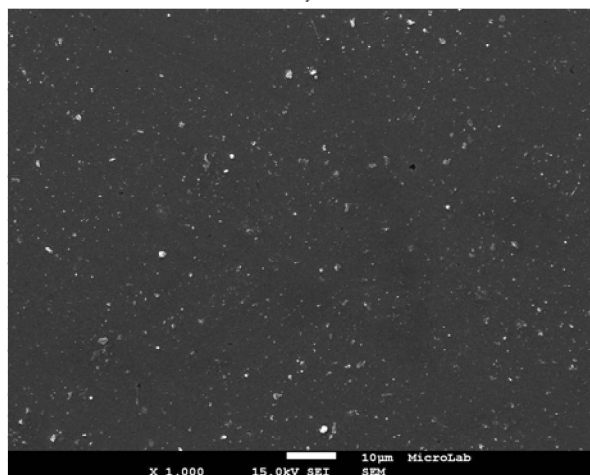
c)



d)



e)



f)

Figure 4.7 – SEM images at 1000x magnification for different substrate temperatures: a) 100°C, b) 200°C, c) 300°C, d) 350°C, e) 400°C and f) 500°C

Figure 4.8 shows a zoomed image of two of these particulates and their brightness is due to the charging effect caused by their poor contact with the rest of the film.

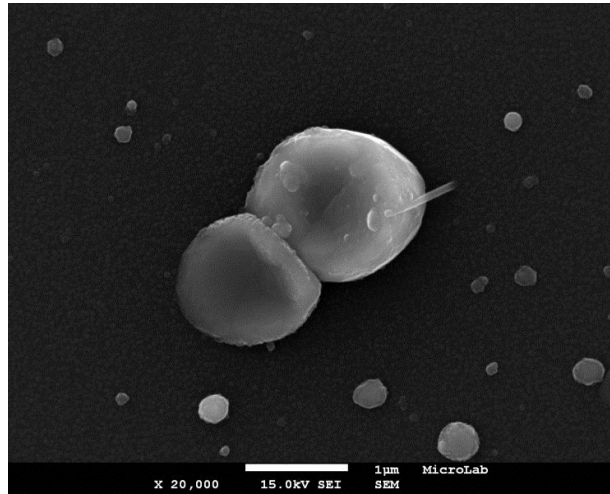
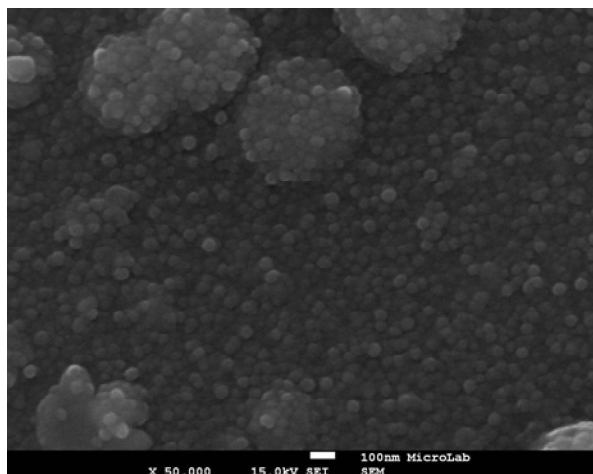


Figure 4.8 – Target-originated particulates

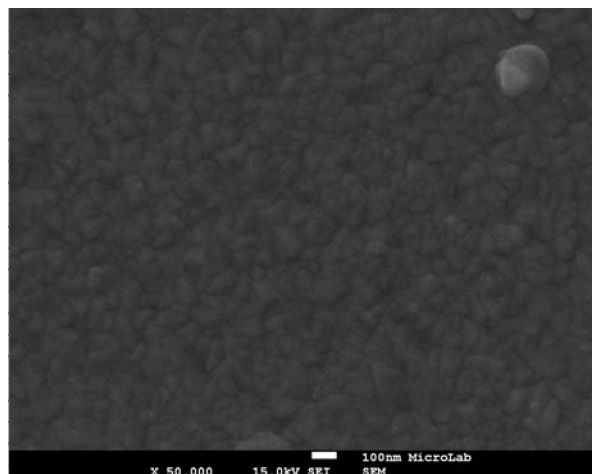
Figure 4.9 shows the SEM images at a nanometric scale. The films are crack free and densely packed. It is also clear that the grain size varies with the temperature. The estimated grain sizes are presented in Table 4.4. The grain size first increases with increasing temperature until the 300°C and decreases for higher temperatures.

Sample	Substrate Temperature	Grain size
	°C	nm
ZnN32	100	40
ZnN33	200	70
ZnN34	300	90
ZnN39	350	30
ZnN35	400	20
ZnN37	500	50

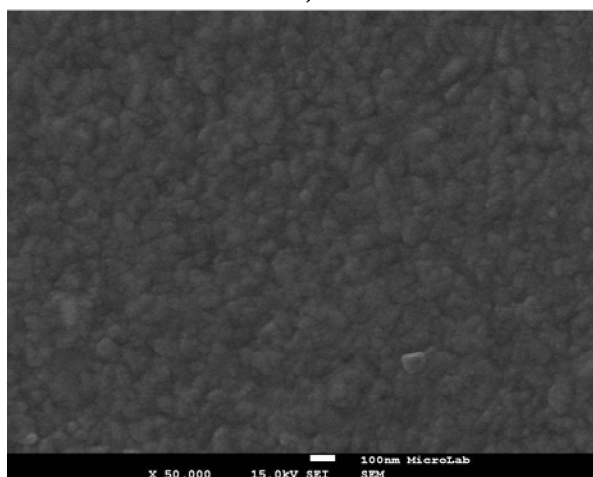
Table 4.4– Estimated grain size variation with the temperature



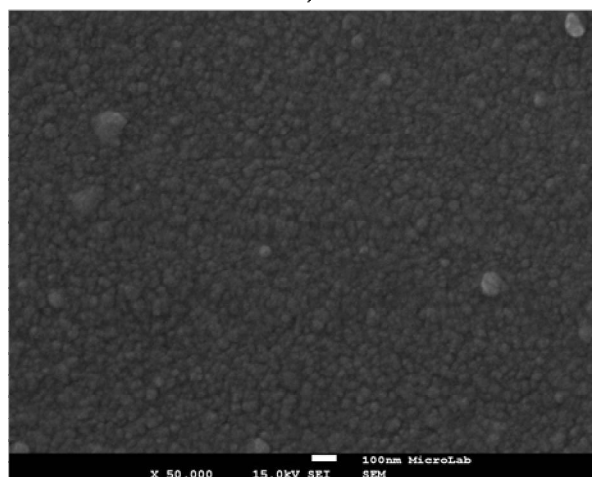
a)



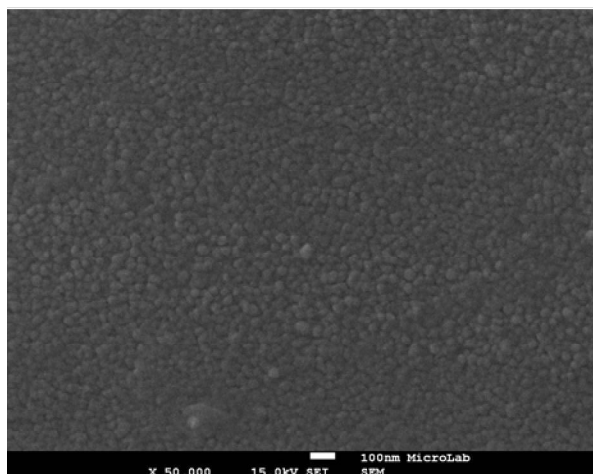
b)



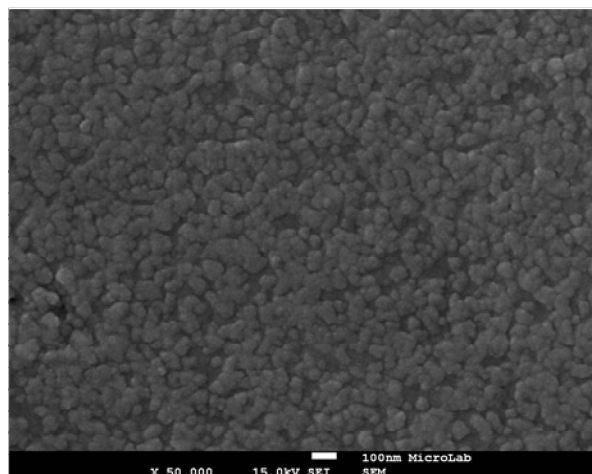
c)



d)



e)



f)

Figure 4.9 - SEM images at 50,000x magnification for different substrate temperatures: a) 100°C, b) 200°C, c) 300°C, d) 350°C, e) 400°C and f) 500°C

4.2.2 Optical Properties

Transmission measurements were undertaken for each sample and the transmittance is plotted in Figure 4.10.

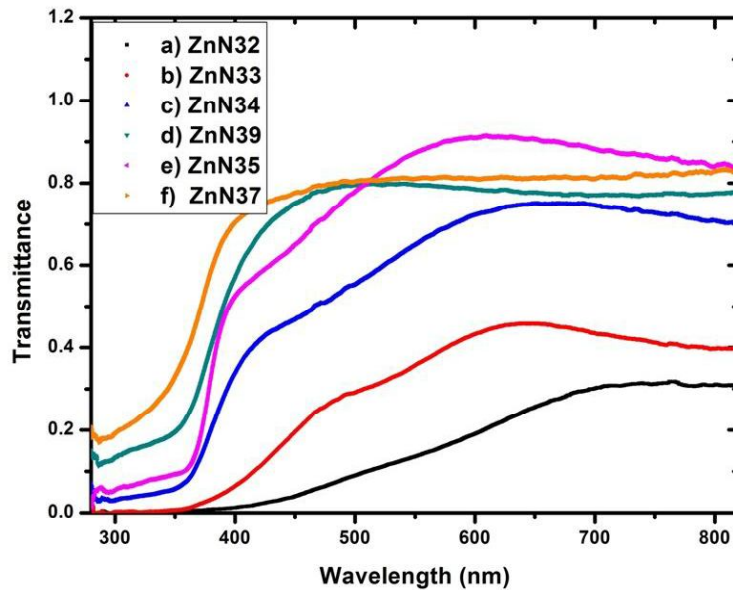


Figure 4.10 – Transmittance spectrum for different substrate temperatures: a) 100°C, b) 200°C, c) 300°C, d) 350°C, e) 400°C and f) 500°C

There is an apparent correlation between the substrate temperature and the film transmission. The higher the substrate temperature the higher the estimated transmittance. Phenomena such as the light scattering and reflection may prevent the light to transmit through the film and are extremely dependent on the film morphology, which is highly dependent on the substrate temperature. It should also be considered the fact that at lower temperatures there is a higher contamination of target-originated particles at the surface and lower nitridation. As these particles are metallic on the inside, they prevent the transmission of the light through that area of the film.

As the temperature rises, it is also visible that the shape of the curves approach a step function, determined by the optical band gap, typical of an ideal semiconductor. However, the plateau seen at lower wavelengths also increases with increasing temperature that may be due to lower film thickness.

All these behaviours have however one exception which is sample ZnN39 (350°C).

The correlation of the transmittance beyond the band gap with the substrate temperature is in accordance with the consulted literature.

The determination of the optical band gap was undertaken using the method described in Section 3.4. This was done assuming a direct band gap, as described by the majority of the literature. Hence, we plotted T^{-2} versus the energy of the incident photon and took the intersection of the linear part of the graph plot with the energy axis to get an estimate of the energy gap. Figure 4.11 illustrates the procedure used in this process taking the transmission data of sample ZnN34.

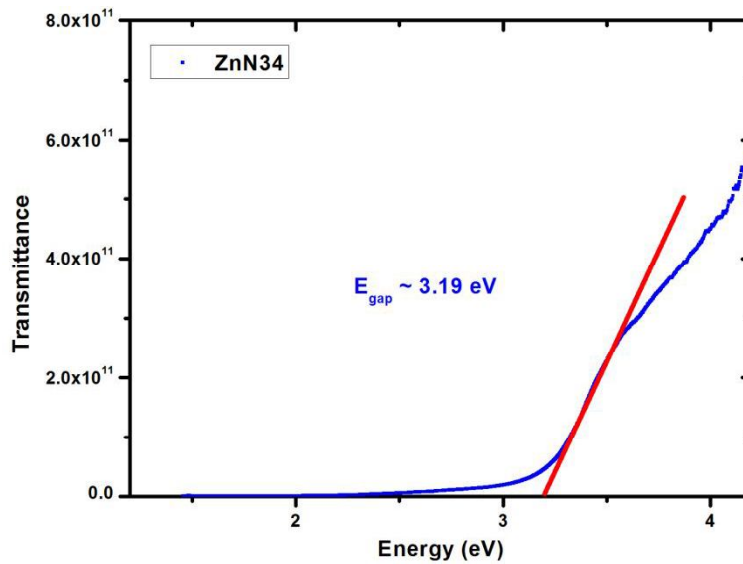


Figure 4.11 – Application of Tauc method to the ZnN34 transmission data

The absorption plot for the different samples is presented in Figure 4.12 and the obtained energy gaps are listed in Table 4.5.

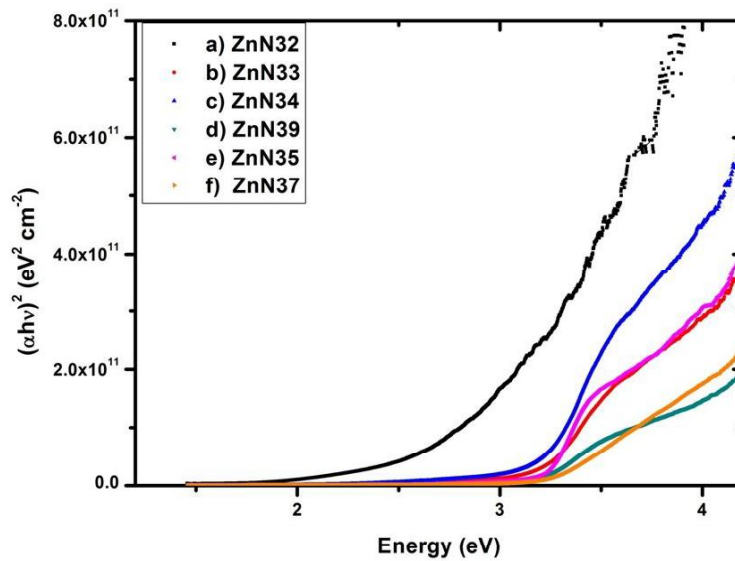


Figure 4.12 – Absorption Plot for different substrate temperatures: a) 100°C, b) 200°C, c) 300°C, d) 350°C, e) 400°C and f) 500°C

In Figure 4.1 we can confirm that the light absorption depends on the substrate temperature. The determined energy gaps are very similar among them and are on average 3.22 eV. The ZnN32 sample, however, has a rough surface and excessively high density of metallic Zinc particles at the surface thus deeply affecting its band gap. Besides this, no major correlation of the band gap and the substrate temperature seems to exist.

Sample	Temperature	Energy gap
	°C	eV
ZnN32	100	2.78
ZnN33	200	3.23
ZnN34	300	3.19
ZnN39	350	3.20
ZnN35	400	3.23
ZnN37	500	3.25

Table 4.5 – Energy gap determined with the Tauc method

The determined band gaps are closer to the second group of values mentioned in Section 2.2 and are near the tabulated Zinc Oxide band gap (3.3 eV). From this characterization method we can infer that there is possibly Zinc Oxide in our films caused by the Oxygen contamination at the film surface. This phenomenon is due to the hygroscopy of Zinc Nitride that has been extensively reported by the literature [29]. Taking in consideration that Zinc Oxide has a high absorption coefficient, this surface contamination may lead to a miscalculated energy band gap.

4.2.3 Structure

X-ray diffraction was done to all the samples and the scan range was set to 20-60°. In Figure 4.13 are plotted the corresponding diffraction patterns. The vertical scale is logarithmic with range [30; 3000]. In that Figure, one can note the presence of two main peaks: one at 34.4° and the other at 36.8°. Both peaks have been reported by the literature to correspond to the Zinc Nitride diffraction pattern [34].

At low substrate temperatures, the 36.8° peak is predominant. This peak corresponds to the (400) Miller plane and is tabulated to exist on both the Zinc Nitride [34] and Zinc spectra [35]. However, it is predominant in the metallic Zinc spectrum and can thus be used as a strong indication of the presence this element in the film. This peak preponderance in our spectra decreases as the temperature rises. This phenomenon may be explained by the fact that at higher temperatures the nitridation of the ablated species is more likely to occur. In addition, at low temperatures, as seen in the SEM images, there is a high density of Zinc particles at the film surface and the high intensity of the (400) peak may also be due to this fact.

The 34.4° peak thus gains relative intensity for higher substrate temperatures which may be assumed to be caused by a higher presence of Zinc Nitride in the film. This effect is particularly noticeable for temperatures beyond 350°C, leading to the assumption that a true Zinc Nitride films are only produced by PLD beyond this point.

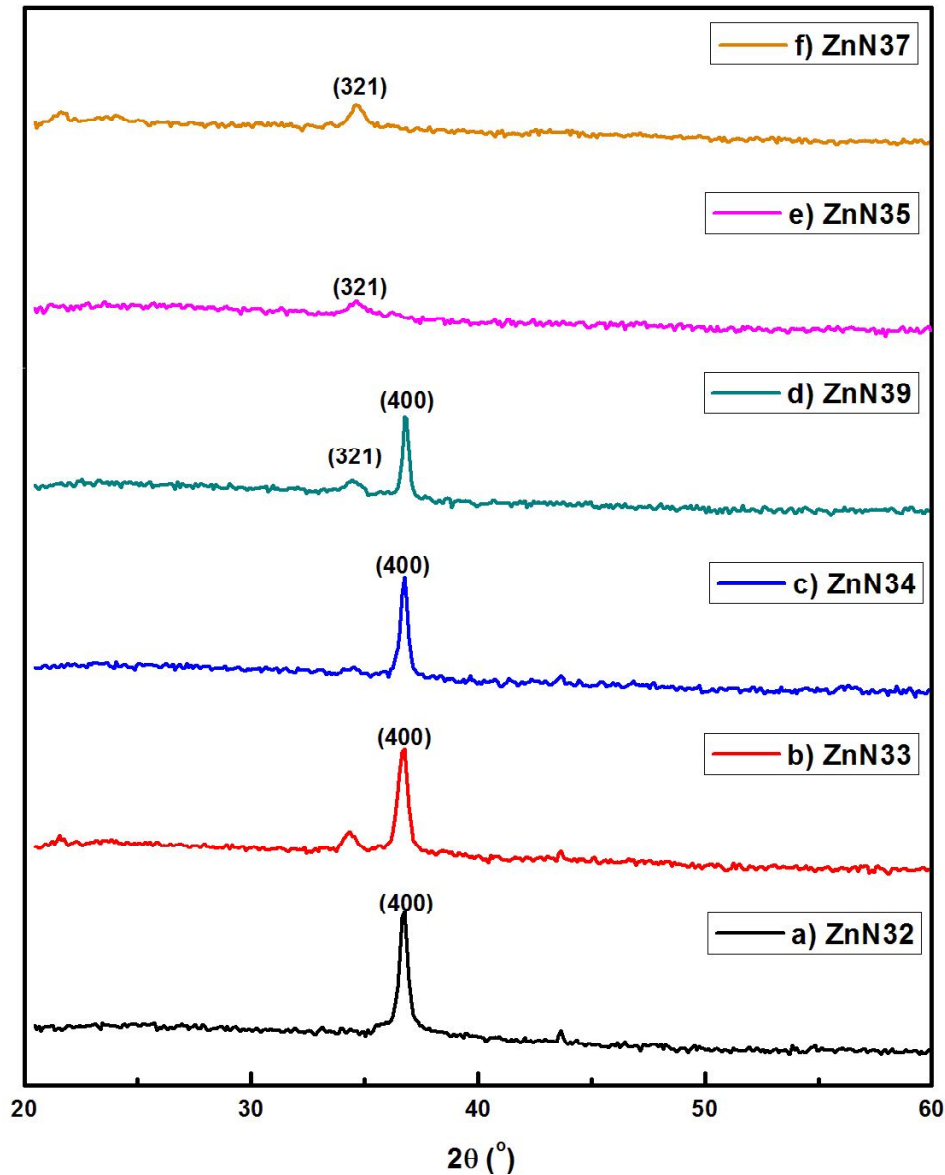


Figure 4.13 - XRD spectrum for different substrate temperatures: a) 100°C, b) 200°C, c) 300°C, d) 350°C, e) 400°C and f) 500°C

The structural properties dependence on the substrate temperatures follows the same trend as the consulted literature, where the (321) peak also gains preponderance with increasing substrate temperatures in detriment of the (400) peak.

The crystal size of the samples with temperature above 200°C was computed by estimating the Full Width at Half Maximum (FWHM) of the (321) peak and using Equation 3.6. The crystal size in the (321) orientation variation with the temperature is shown in Figure 4.14. This parameter first decreases with increasing temperature until the 350°C temperature and increases beyond that point. This observation corroborates the hypothesis that 350°C is a turning point in the Zinc Nitride film deposition.

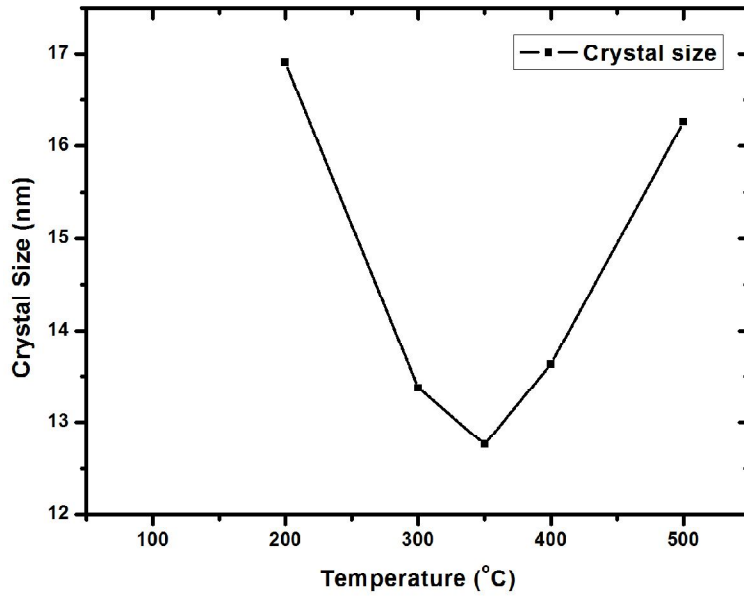


Figure 4.14 – Crystal size variation with the substrate temperature

4.2.4 Electrical Properties

I-V measurements were then carried out. Since every sample demonstrated a purely ohmic conduction, the resistivity was determined by the method mentioned above.

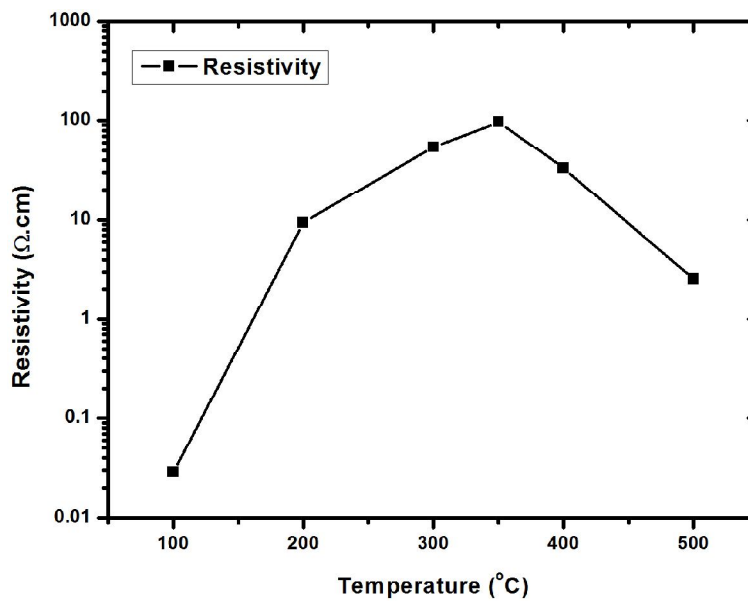


Figure 4.15 – Resistivity temperature dependence

Figure 4.15 shows the resistivity as a function of the substrate temperature. The curve has its maximum at 350°C. This behaviour may be explained by the different ratio metal/semiconductor on the film. At low temperatures, there is a high density of metallic Zinc which facilitates the passage of current through the film. As the temperature rises, there are fewer particles and the resistivity increases reaching its maximum at 350°C. From this point on, as seen previously, occurs an effective

production of Zinc Nitride films and the structural properties improve causing the decrease of the resistivity.

Furthermore, the resistivity variation with the temperature is coherent with the crystal size variation displayed in Figure 4.14. This might be explained by the fact that lower crystal sizes generate a higher number of potential barriers that the signal has to overcome to flow through the film.

These are generally higher resistivities than the results reported by the literature where the range was 10^{-3} - 10^{-1} . Also, the temperature dependence is similar but the peak is at 350°C whereas in the literature is at 100°C.

4.3 Oxygen Contamination

XPS measurements were performed to samples with two different substrate temperatures (300°C and 400°C) and the other deposition conditions were similar to the previously studied samples. Figure 4.16 shows typical wide scan XPS spectrum of as deposited thin film, in the binding energy range of 0–1200 eV. As it can be seen, four main elements were found in this analysis: Carbon, Oxygen, Zinc and Nitrogen. The presence of Carbon is justified by the typical contamination of this element at the surface of samples that were in contact with the atmospheric ambience. Oxygen contamination at the film surface also occurs, which is in agreement with the literature and our previous assumptions. A low percentage of Nitrogen was detected. However, this element is difficult to detect mainly due to its low XPS sensitivity.

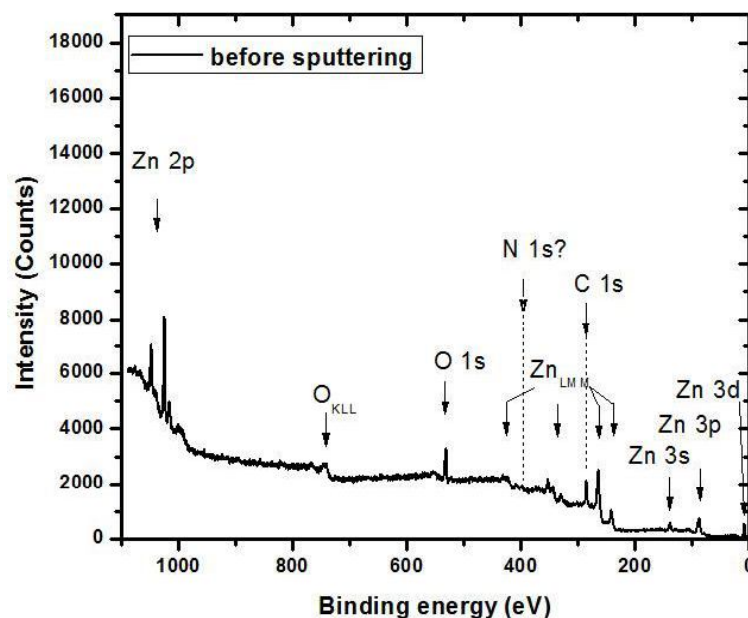


Figure 4.16 – XPS spectrum for substrate temperature of 300°C

Atomic concentrations, reported in Table 4.6, were determined from the photoelectron peak areas using Shirley background subtraction and sensitivity factors provided by the instrument manufacturer.

Substrate Temperature (°C)	Composition (%)			
	C	O	Zn	“N”
300	19.1	40.1	36.6	4.2
400	27.4	47.7	22.3	2.6

Table 4.6 – Sample surface composition

After this first analysis, sputtering was done to the sample with substrate temperature of 300°C. Argon was used to remove the first layers of material and to do a deeper analysis. This process was done in two steps: first with 20 cycles and afterwards another 40 cycles.

Figure 4.17 shows the XPS spectrum before sputtering, after 20 and 40 sputtering cycles. These last two curves are fairly similar to each other and different from the surface spectrum. The obtained sample composition is displayed in Table 4.7.

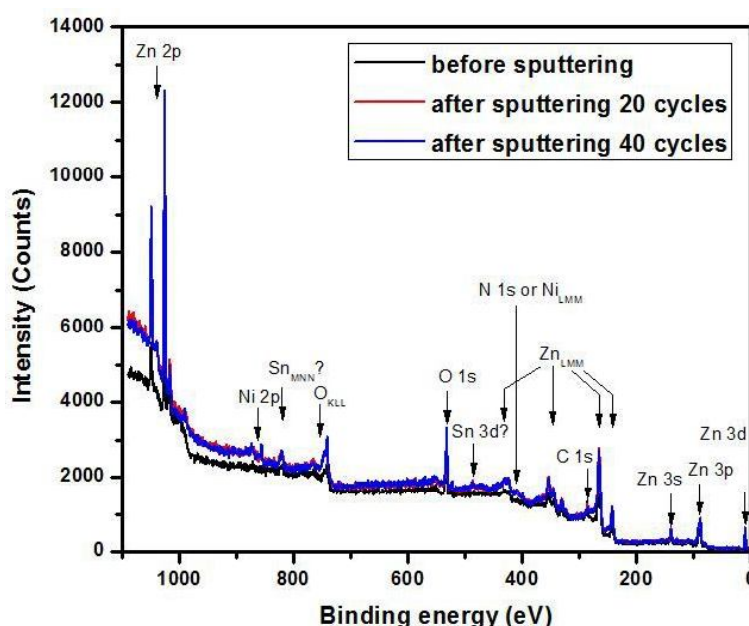


Figure 4.17 - XPS spectrum for substrate temperature of 300°C before sputtering, after 20 cycles and after 40 cycles of sputtering

	Composition (%)			
	C	O	Zn	“N”
Before sputtering	19.1	40.1	36.6	4.2
After sputtering	13.6	35.6	32	18.8

Table 4.7 – Sample composition before and after sputtering

A decrease in the Carbon, Zinc and Oxygen predominance is clear and Nitrogen apparently gains preponderance. However the XPS sensitivity does not allow guaranteeing that the observed peak corresponds to the Nitrogen. In addition, it is important to take into consideration the fact that, even though sputtering was done, we are still analysing the first layers of the sample as is testified by the

high percentage of Carbon detected. Moreover, it has been reported that sputtering done with Argon gas does a preferential sputtering to the Nitrogen atoms [37,38].

The previous analysis confirms the presence of Oxygen on our film surfaces. This is coherent with the literature and may be the cause of the high optical band gap obtained previously. A further sputtering treatment would be necessary to understand how deep the Oxygen contamination reaches.

Chapter 5

Results on MIS and TFT Production

5.1 MIS results

In Chapter 2 we established the different layers necessary to produce a Thin Film Transistor. Besides the semiconductor layer it is necessary to include an insulator and a Gate electrode. In this Section we study three structures to possibly be used as substrates of our TFTs test structures: Glass+ITO+ATO, AlN+Si - 1 and AlN+Si - 2. The three structures had Aluminium deposited on top of the insulator to form a true MIS structure.

The ATO+ITO structure is composed by a metal layer of Aluminium, an insulator layer of Aluminium-Titanium-Oxide (ATO) with 200 nm thickness and a semiconductor layer of Indium Tin Oxide (ITO).

The AlN+Si structures are composed by a metal contact (Aluminium), an insulator layer of Aluminium Nitride (AlN) with thickness of approximately 200 nm and a semiconductor layer of p-type doped Silicon.

To better understand these structures behaviour and to decide if they are viable to be used as TFTs substrates, a set of measurements was made. The measurements done were transversal I-V and C-V curves.

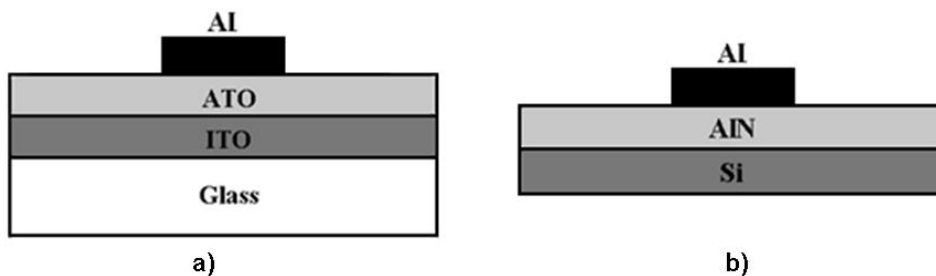


Figure 5.1 MIS structures: a) Al+ATO+ITO b) Al+AlN+Si 1/2

5.1.1 I-V Characteristics

Figure 5.2 shows the transversal I-V curves of the three MIS. As predicted in Section 2.3.2, even though ideally an insulator should not allow any charge flow through it, in real insulators that is not the case. In the transversal I-V curve of the three structures, there is, in fact, current flow through the insulators. The substrates show two different behaviours: AIN+Si - 1 shows a Schottky barrier and the AIN+Si - 2 and the ATO+ITO show ohmic conduction.

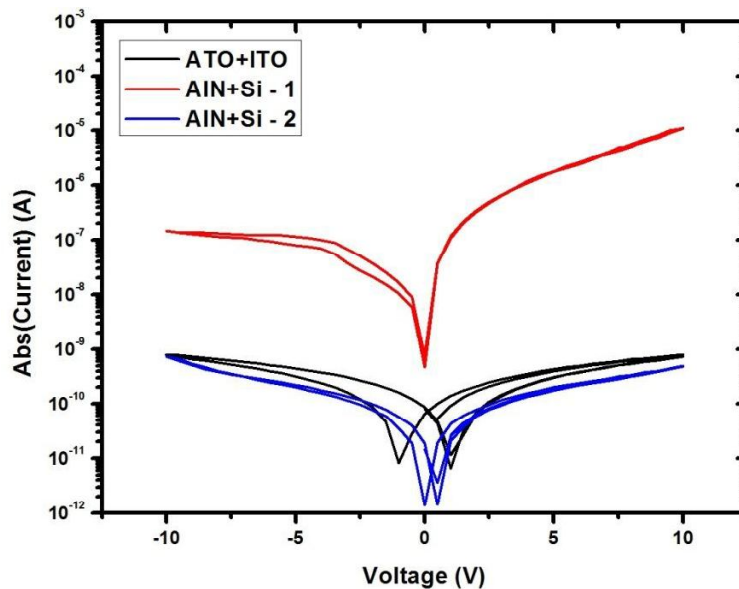


Figure 5.2 Transversal I-V Curves of the MIS structures

For the AIN+Si - 1, besides the fact that there is a Schottky barrier, the current reaches values up to 10^{-5} A. This is a relatively high leakage current that might compromise the performance of a TFT device.

Concerning the ATO+ITO and AIN+Si - 2, both curves show an ohmic characteristic with high resistance. We can also clearly observe a hysteresis on both curves that may be caused by several reasons: presence of charges in the insulator or the interface, return of the uncompensated donors to the original positions and so on. A higher hysteresis was detected in the ATO+ITO structure.

5.1.2 C-V Characteristic

The C-V curve of the three substrates is shown in Figure 5.3. The AC signal had a frequency of 1 kHz and amplitude of 100mV.

For AIN+Si (1 and 2) substrates, we obtain a typical behaviour of a p-type MIS structure. At negative voltages, the device is in accumulation. As the voltage increases, there is a depletion of the majority carriers (holes) from the insulator-semiconductor. With a higher voltage, the minority carriers (electrons) are attracted to the interface and there is inversion. Considering that the AC signal had a relatively high frequency, the electrons do not have time to respond to it and the device does not enter the strong inversion region of operation.

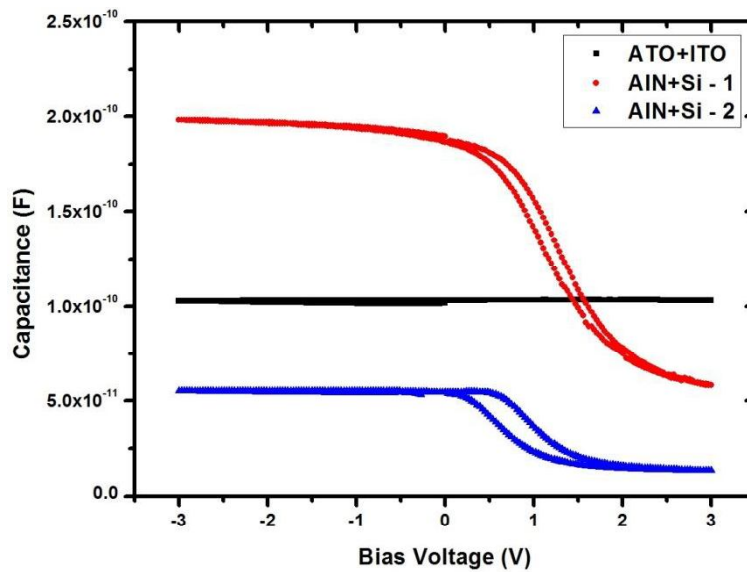


Figure 5.3 C-V curves of the MIS structures

Concerning the ATO+ITO, there is no significant variation of the capacitance with different bias voltage. This may be explained by the fact that the ITO has a very high conductivity and behaves almost as a metal. This C-V curve is thus simply the result of a two plate capacitor with the ATO acting as dielectric and the ITO and Al as the two plates.

5.1.3 MIS choice

Considering the electrical properties shown above, it was decided to use the ATO+ITO and AlN+Si – 2 as substrates of the TFT. ATO and AlN will be the insulators and ITO and Si will be the Gate electrodes on our structures.

5.2 Zinc Nitride Deposition Conditions

A Zinc Nitride layer of approximately 150 nm thickness was deposited on top of the substrates previously chosen to act as the channel layer of the TFT. The deposition parameters were chosen so as to optimize the device performance.

The laser wavelength was set to 532nm (green) for all the reasons previously explained. Concerning the substrate temperature, we took into consideration the film morphology, structural, optical and electrical properties. Considering that the films studied in the previous Chapter showed modest properties for temperatures bellow 350°C, two substrate temperatures were thus used to produce the Zinc Nitride layer of our TFT test structures: 400°C and 450°C.

5.3 Contact geometry

The Aluminium Source and Drain contacts, necessary for the TFT structures, were done using the thermal vaporization method (Section 3.2) and masks. These contacts are approximately 150 nm thick and have the following geometry:

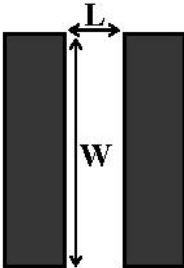


Figure 5.4 – Source and Drain contact geometry

To maximize the Drain-Source current and improve the TFT performance, according to Equation 2.6, it is necessary to maximize the Width/Length ratio. Thus, the W/L ratio was set to: 4000 μm /750 μm .

5.4 TFT structure

The final TFT test structures in staggered bottom-gate configuration are shown in Figure 5.5.

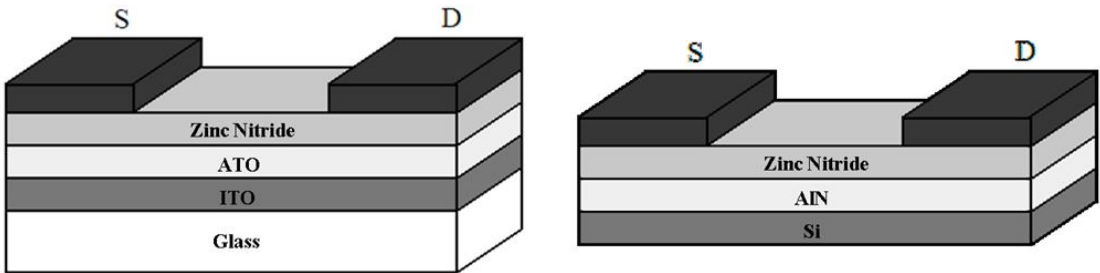


Figure 5.5 TFT test structures configuration

Chapter 6

Results on TFT Operation

TFTs test structures were produced depositing Zinc Nitride films on top of two substrates (ATO+ITO and AlN+Si - 2) with two substrate temperatures (T_s): 400°C and 450°C. The analysis of the obtained results will be divided by their substrates. The following nomenclature will be used throughout this Chapter:

- ATO+ITO substrate: ATO400 ($T_s=400^\circ\text{C}$) and ATO450 ($T_s=450^\circ\text{C}$)
- AlN+Si:: AlN400 ($T_s=400^\circ\text{C}$) and AlN450 ($T_s=450^\circ\text{C}$)

SEM images, optical and electrical measurements were performed of the films, showing similar properties to the ones described in Chapter 4.

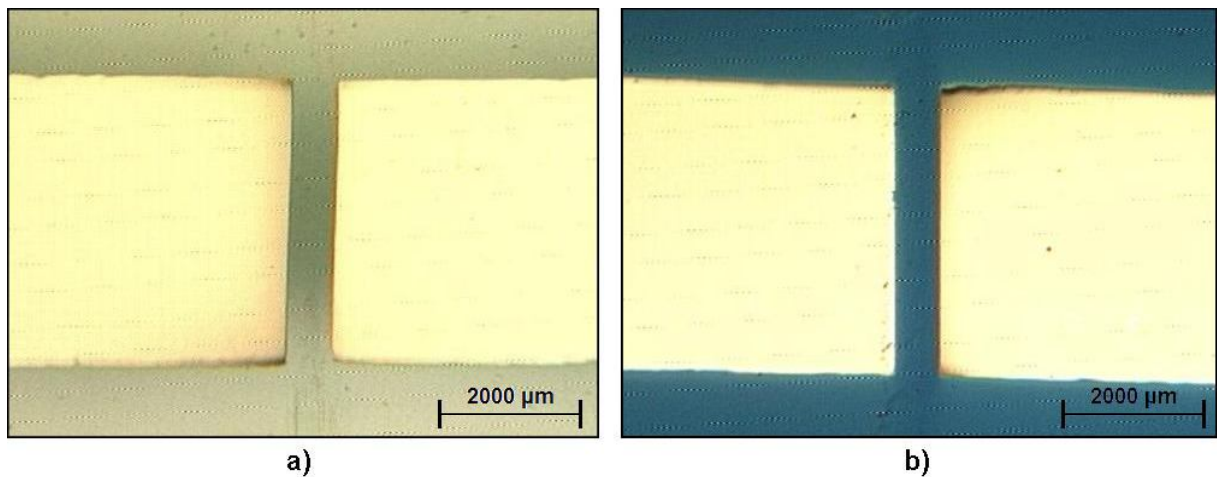
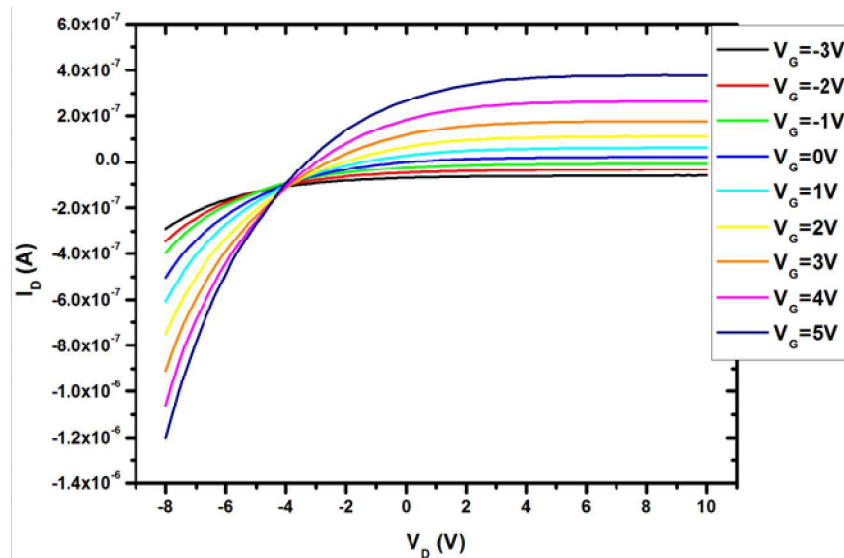


Figure 6.1 – Optical Microscope images of the Source and Drain contacts a) ATO+ITO substrate
b) AlN+Si substrate

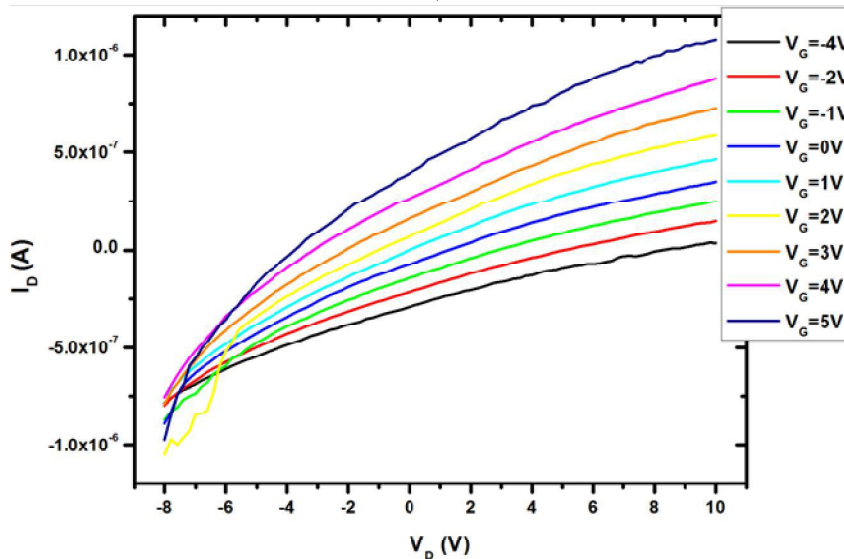
6.1 TFT on ATO+ITO Substrate

6.1.1 Output characteristics

Figure 6.2 shows the output characteristics of the TFTs produced with ATO+ITO as the substrate and with the two different substrate temperatures during deposition. The two plots have very different characteristics between each other and they deviate from typical output characteristic of a typical TFT.



a)



b)

Figure 6.2 - Output Characteristics of the TFTs: a) ATO400 b) ATO450

The ATO400 shows diode-like curves with increasing currents as the Gate voltage increases. The intersection of the different curves occurs at $V_D \sim -4$ V. For further negative Drain voltages, particularly for high Gate voltages, there is a high Drain-Source current up to microamperes.

The ATO450 sample shows several square-root-like curves with higher slopes for higher Gate voltages, as expected in the linear region of a TFT. However, almost no saturation can be seen and the lines intersect at Drain voltage of -8V.

On both of these plots we notice a strong influence of a leakage current from the Gate electrode (ITO), through the insulator (ATO) onto the semiconductor layer (Zn_3N_2). This current seriously compromises the device operation.

Taking the Drain-Source currents at zero Drain voltage, we can estimate the leakage current for different Gate voltages and obtain a rough estimation of the post-deposition ATO resistance of 10 M Ω . Comparing the transversal I-V curves showed in Section 5.1.1, we see that the resistance decreases by about two orders of magnitude after the deposition.

It is important to notice that we do not observe complete short-circuits in perpendicular direction, since the resistance is still about 10000 times larger than typical short-circuit resistance values of Zn_3N_2 deposition, the dielectric layer has obviously suffered some deterioration, as we will discuss below.

The occurrence of leakage currents across ATO layers had also been reported by the literature [18,19].

6.1.2 Transfer characteristics

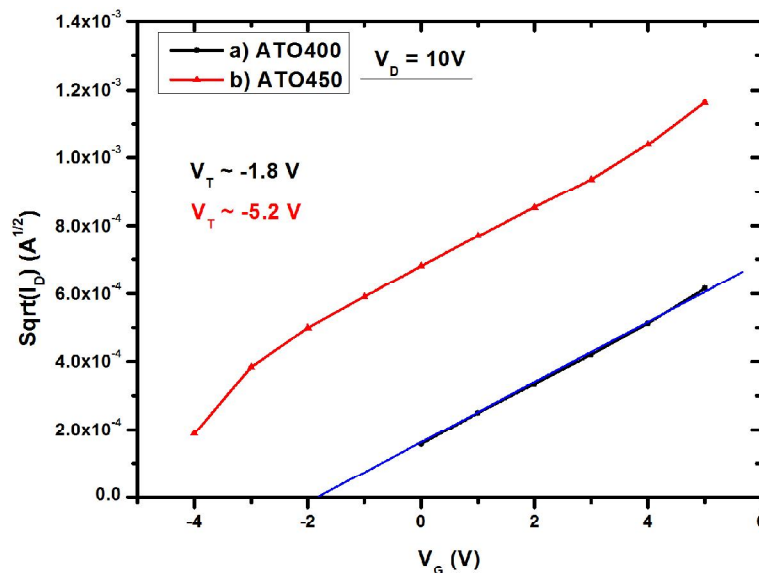


Figure 6.3 – Square-root Transfer Characteristics at saturation of the TFTs: a) ATO400 b) ATO450

Figure 6.3 shows the square-root transfer characteristic of both TFTs. A linear behaviour is observable on both curves. The extrapolated threshold voltages are -1.8V for the ATO400 and -5.2 V for the ATO450. Since these are n-type TFTs, the threshold voltages indicate that these are depletion-mode transistors as it is also apparent from Figure 6.5.

The logarithmic transfer characteristics displayed on Figure 6.4 allowed us to estimate the ON/OFF ratio and the sub-threshold swing for both TFTs. Both TFTs have a low amplification power as demonstrated by the sub-threshold voltage swing values (3 and 6 V/decade). The on/off ratio has a low value as a result of the leakage currents that exist in these devices.

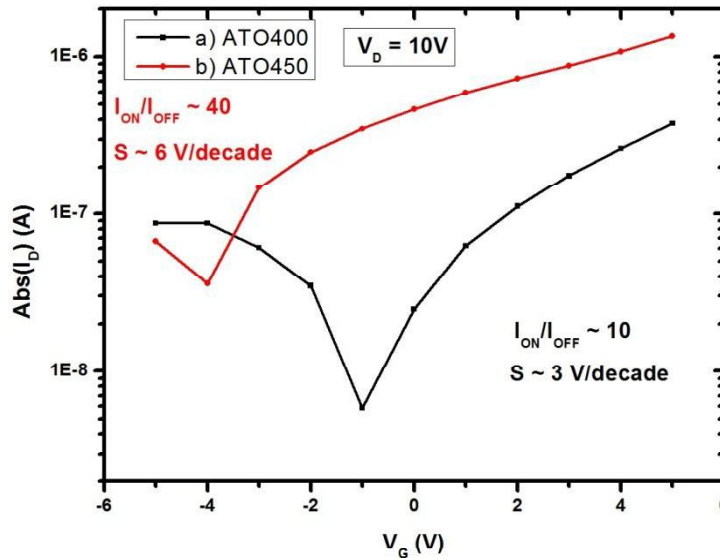


Figure 6.4 - Logarithmic Transfer Characteristics at saturation of the TFTs: a) ATO400 b) ATO450

The device mode of operation detected is similar to those obtained with a back-to-back diode configuration, typical of a Bipolar Junction Transistor (BJT). More work would be needed to fully analyse those models which are commonly adopted in electrotechnical circuit simulation, which is outside the present work focus.

6.2 TFT on AlN+Si-2 Substrate

6.2.1 Output characteristics

Figure 6.5 shows the output characteristics of two TFTs produced on top of the AlN+Si - 2 substrate deposited at different substrate temperatures. Comparing to Figure 2.9, we can see a FET-like behaviour. The Drain-Source currents increase with increasing Gate and Drain voltages and the saturation of the Drain-Source current as the Drain voltage gets closer to the Gate voltage also occurs. However, there are several deviations from the ideal case presented in Section 2.4.1. We will discuss some of them in the following paragraphs.

Two main characteristics of these plots have drawn our attention: relatively high I_D currents for zero and negative Drain voltages. At both of these conditions, only a negligible current should be able to pass through the Zinc Nitride film given that at this region there should be no induction of channel at the semiconductor-insulator interface. However, that is not the behaviour that we observe on both of these plots. For V_D in the range $[-8, 0]$ V, non-zero currents that clearly increase with increasing Gate and Drain voltages are visible. This effect is particularly noticeable for the output characteristic shown in Figure 6.5b).

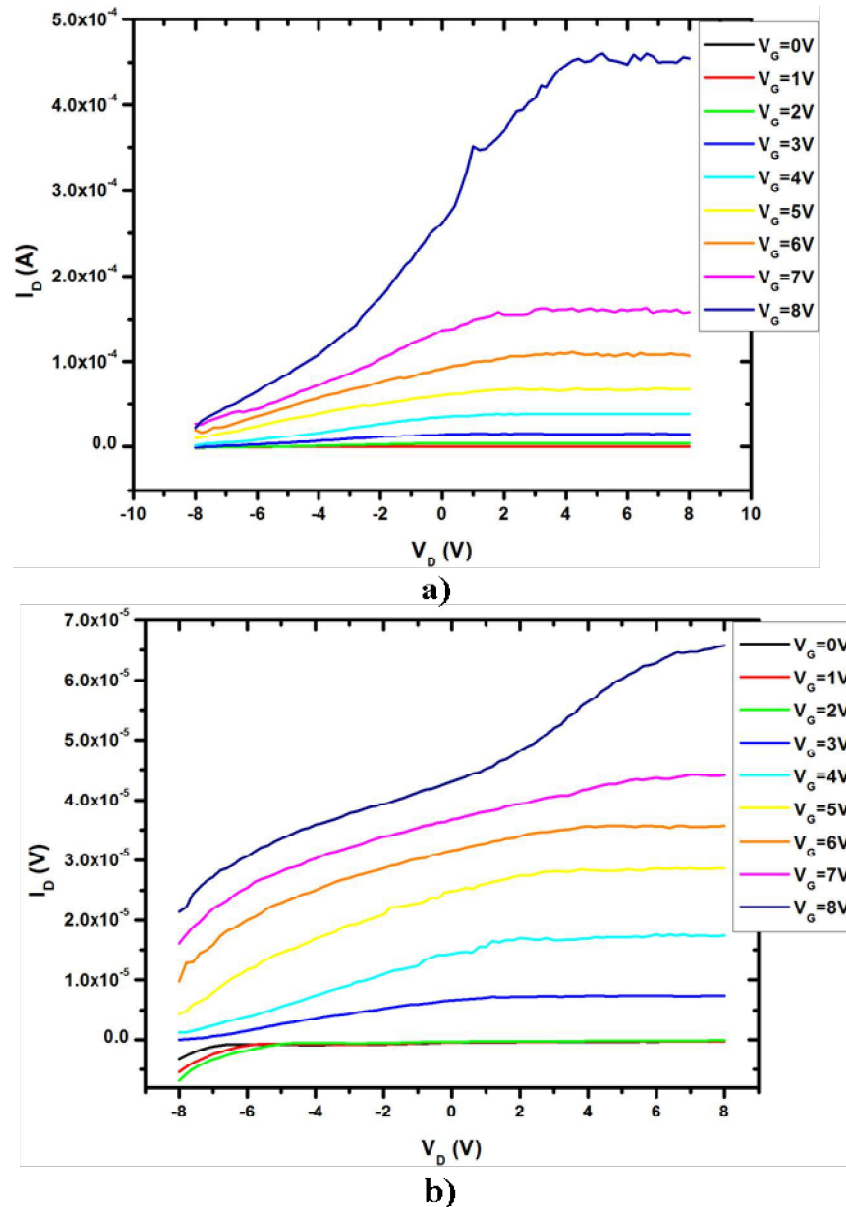


Figure 6.5 – Output Characteristics of the TFTs: a) AIN400 b) AIN450

The existence of a leakage current through the insulator (AIN) may be one of the causes of such behaviour. As it has been explained in Section 2.1.2, the PLD production method has the tendency to damage the substrates and the substrate-film interface caused by the incidence of high energy particles. These species bombardment compromises the interface and the substrate itself primarily by two phenomena: implantation on the substrate and unintentional sputtering. These likely occurred on our film depositions particularly taking into consideration that a metallic target was used. As we saw in Chapter 4, micrometric size particles appeared on our deposited films having thus a larger size than the total insulator thickness. Consequently, the particle implantation and unintentional sputtering may have affected not only the substrate-film interface but also the insulator layer almost to its full thickness.

The phenomena mentioned above may thus have caused defects, local short-circuits, traps, amongst others on the Aluminium Nitride layer irreversibly damaging it. So, when a voltage is applied

to the Gate electrode, a leakage current is able to pass through the insulator onto the Zinc Nitride layer, inducing an extra unwanted current and an offset to the output characteristic.

Assuming that the leakage current has an ohmic-like behaviour, the shunt resistance through the insulator at $V_D=0V$ is approximately $0.1M$. This value is three orders of magnitude below the resistance obtained in the analysis previously done to the MIS structure. This observation corroborates the hypothesis that the AlN layer was damaged during the deposition. However, this is a rough estimation as we can observe in Figure 6.5a) that this effect is not directly proportional to the applied Gate voltage.

As mentioned in Section 2.4.2, the existence of alternative current paths strongly influences the TFT operation. The TFT output characteristic shown in Figure 6.5a) has a better performance than the one shown in Figure 6.5b). This fact is probably due to lower leakage currents, allowing the Drain-Source currents to show a more FET-like behaviour.

6.2.2 Transfer characteristics

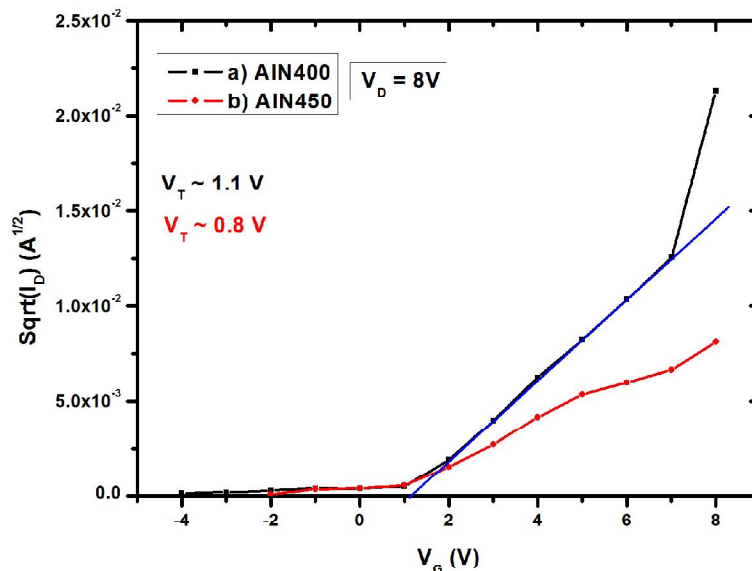


Figure 6. 6 – Square-Root Transfer Characteristic at the saturation region of the TFTs: a) AIN400
b) AIN450

The square-root transfer characteristics at saturation ($V_D = 8V$) are displayed in Figure 6.6 showing a typical FET behaviour. The threshold voltages were estimated by intercepting the linear part of the curve with the abscissas axis. For the AIN400 sample a $V_T = 1.1V$ and for AIN450 a $V_T = 0.8V$. Seeing that these values are positive and that this is an n-type TFT, the TFTs should both be enhancement-mode transistors. However, this is not in accordance with the output characteristic previously displayed that may, once again, be justified by the leakage currents observed.

Assuming an unaltered insulator capacitance than the value estimated in the previous Chapter, the carrier mobility was computed. The Field-Effect mobility was obtained using Equation 2.11 and the slope of the transfer characteristic for $V_D=3V$. The Field-Effect mobilities were: $0.6 \text{ cm}^2V^{-1}s^{-1}$ for the AIN400 and $0.1 \text{ cm}^2V^{-1}s^{-1}$ for the AIN450. The saturation mobility was obtained by taking the slope of

the linear part of the previous plot and using Equation 2.11. The estimated saturation mobilities were: $1.1 \text{ cm}^2\text{V}^{-1}\text{s}^{-1}$ in the AIN400 and $0.3 \text{ cm}^2\text{V}^{-1}\text{s}^{-1}$ in the AIN450.

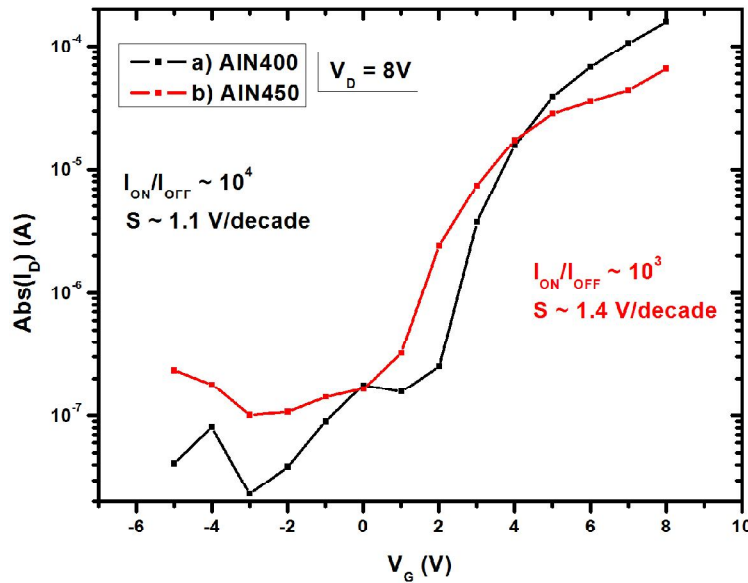


Figure 6.7 – Logarithmic Transfer Characteristic at the saturation region of the TFTs: a) AIN400
b) AIN450

Figure 6.7 shows the logarithmic transfer characteristic. The On/Off ratio is 10^4 and 10^3 for the AIN400 and AIN450, respectively. These are modest values probably resulting from the leakage current that does not allow a better on/off state separation.

The sub-threshold swing (S) was estimated using Equation 2.10 and is approximately 1.1V/decade and 1.4V/decade for the AIN400 and AIN450. Hence, it is necessary to apply more voltage to the Gate electrode of the second TFT to achieve one decade amplification.

In general, the previously stated results demonstrate that Zinc Nitride is a good candidate to be used as channel layer in TFT production. The TFT test structures with AIN+Si as substrate showed a FET-like behaviour with two clearly demarked operation regions: linear and saturation. The Gate voltage clearly influences the coplanar currents with a reasonable amplification power as demonstrated by the sub-threshold swing parameter obtained. Out of all the test structures produced, the AIN400 TFT showed the best TFT operation.

However, leakage currents caused by substrate damage during the deposition prevent an optimal performance of these test structures. Performance evaluation parameters were thus severely influenced by this behaviour. A complete study of the interface structure would be necessary to have a better understanding of the occurring phenomena. A further optimization of the Zinc Nitride thin film deposition to completely avoid the impinging of high energy species on the substrate and film would also be necessary.

Comparing with the TFTs reported by the literature we observe that the evaluation parameters, namely the mobility and the threshold voltage, as well as the drain currents achieved are within the previously reported range.

Chapter 7

Conclusion and Future Work

7.1 Conclusion

All the goals established for this work were accomplished: the study of the Zinc Nitride deposition by PLD, the development of an auxiliary Labview-based program and the production of TFT Zinc Nitride based test structures

A Labview-based program was developed for this work. The program essentially sends commands to a lock-in amplifier to stipulate the voltage applied to the DUT and afterwards collects the current measured by a picoammeter. This program helped to ease the measurement workload and save time.

Zinc Nitride films were grown by Pulsed Laser Deposition (PLD). The influence of two essential deposition parameters (laser wavelength and substrate temperature) on the film properties was studied. Both parameters were proven to have a strong influence.

Concerning the laser wavelength, the Nd:YAG laser system could be operated in the basic mode in the infrared at 1064 nm, in second-harmonic generation at 532 nm, and in fourth-harmonic mode in the UV spectral region at 266 nm. The three laser lines produced very different film properties. The contamination of target-originated particles was dominant for higher wavelengths, as predicted by the literature. On the other hand, the power of the laser as it hits the target also increased with the wavelength. The green line (532 nm) was thus concluded to be a good compromise.

As for the substrate temperature, the morphology, the structural, optical and electrical properties of the films varied significantly with increasing temperatures. The presence of target-originated particles was predominantly detected at low substrate temperatures, between 100°C and 300°C. The estimated energy gap was on average 3.22 eV and the resistivity changed in a wide range of 10^{-2} -100 Ω .cm. The analysis of the results led to the assumption that a Zinc compound is only formed by PLD for temperatures beyond 350°C. XPS measurements showed the presence of Oxygen at the film surface, as predicted by the literature.

Three MIS structures were then studied as potential TFT substrates. After evaluating the electrical behaviour of those, it was decided to use to use AlN+Si and ATO+ITO. For deposition temperature

below 350°C the film properties were not adequate for the TFT semiconductor. Test structures of staggered bottom-gate TFTs (without any lithographic patterning of contacts) were then produced with substrate temperatures of 400°C and 450°C and with width/length ratio of 4000 μm/750 μm.

The produced TFTs demonstrate output and transfer characteristics that allowed estimating the On/Off ratio, the threshold voltage shift, and the sub-threshold voltage swing. The characteristics showed some deterioration with respect to ideal curves due to the presence of leakage currents. The coplanar-to-leakage current ratio still needs optimization. However, in this work, we observed that Zinc Nitride is a potential candidate to be used as channel layer in TFT production.

The best values were obtained with AlN-based TFTs where the AlN400 was a threshold voltage of 1.1 V, a sub-threshold voltage swing 1.1 V/decade, an on/off ratio of 10^4 and $0.6 \text{ cm}^2/\text{Vs}$ mobility in saturation.

7.2 Future Work

Several problems were encountered during this work. Some possible solutions will be presented in the following paragraphs.

In Chapter 4, a study of the deposition parameters was made but further optimization is still necessary. The influence of the Nitrogen pressure, for instance, would be interesting to explore.

A compromise decision had to be made in the laser wavelength choice. This was mainly caused by the lower power of the UV line and the power cut-off induced by the quartz port. The use of a higher power UV laser might increase the film quality, inducing less target deformation and less target-originated particles thus producing more uniform films.

Another possible solution to avoid the presence of particles in the film would be the use of a shutter between the target and the substrate. This device would act as a shield, preventing the particle arrival to the substrate. The influence of the subsequent thermal annealing may also be exploited to increase the film uniformity. Another possible solution would be to use sintered targets made from powder either Zinc or Zinc Nitride since it has been reported that metallic targets produce less uniform films.

It seems that the TFT performance was compromised by the damaged done to the highly resistive dielectric layer of the substrate during depositions. Besides the avoidance of high kinetic energy particles to the film, the option of using a thicker and more resistant insulator should be considered. Another possible improvement would be to decrease the contacts area with, for instances, lithography and thus decreasing the alternative current paths.

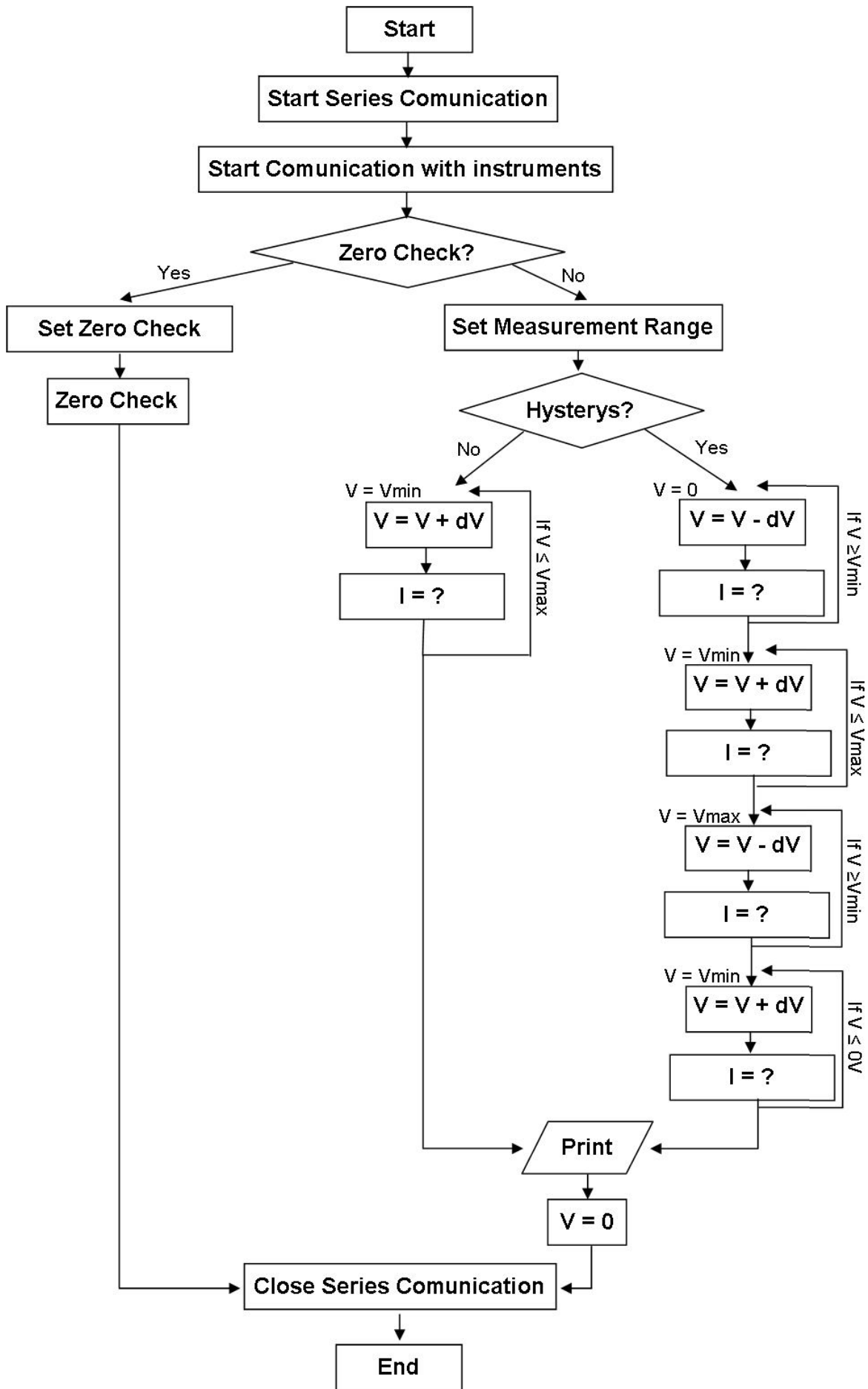
A better understanding of the interface morphology would help to better understand the effects of PLD on those. Atomic Force Microscopy (AFM) and Transmission Electron Microscopy (TEM) would be possible methods to use in this kind of study.

One important aspect of Zinc Nitride production is the presence of Oxygen at film surface. This phenomenon has been extensively studied by the literature, but still no solution has been accomplished. One possibility would be to passivate the film surface in-situ, that is, before the film is taken out from vacuum, using an inert cover layer on top.

Appendix A

I-V Measurements Program - Flowchart

A Labview-based program was developed for this work, its description is displayed in Section 3.3.2 and its flow chart is showed in the next page.



References

- [1] J. E. Lilienfield, U. S. Patent 1745175 (1930)
- [2] J. E. Lilienfield, U.S. Patent 1900018 (1933)
- [3] D. Kahng, M.M. Atalla, Solid-State Device Research Conference, June (1960)
- [4] P. K. Weimer , Proceedings of the Institute of Radio Engineers 50, 1462 (1962)
- [5] H. M. Smith, A. F. Turner, Appl. Opt. 4 ,147 (1965)
- [6] R. K. Singh, D. Bhattacharya, J. Narayan, Appl. Phys. Lett. 57, 2022 (1990)
- [7] R. Ramesh, A. Inam, D. M. Hwang *et al.*, Appl. Phys. Lett. 58, 1557 (1991)
- [8] Y. Watanabe, M. Tanamura, S. Matsumoto, Y. Seki, J. Appl. Phys. 78, 2029 (1995);
- [9] S. Amoruso, B. Toftmann, J. Schou, Phys. Rev. E 69, 056403 (2004)
- [10] A. Sambri, D. V. Cristensen, F. Trier *et al.*, Appl. Phys. Lett. 100, 231605 (2012)
- [11] S. Fähler, K. Sturm, H.U. Krebs, Appl. Phys. Lett. 75, 3766 (1999)
- [12] G. C. Tyrre, T. H. York, L. G. Coccia *et al.*, Appl. Surf. Sci. 96, 769 (1996)
- [13] H. Juza, Z. Hahn, Anorg. Allg. Chem. 224, 125 (1940)
- [14] K. Kuriyama, Y. Takahashi, F. Sunohara, Phys. Rev. B 48, 2781 (1993)
- [15] S. Simi, I. Navasa, R. Vinodkumar *et al.*, Appl. Surf. Sci. 257, 9269 (2011)
- [16] P. Sanguino, "Growth of Gallium Nitride with the Cyclic Pulsed Laser Deposition System", PhD Tesis (2005)
- [17] R. Ayouchi, C. Casteleiro *et al.*, Phys. Status Solidi C 7, 2294 (2010)
- [18] R. Ayouchi, C. Casteleiro *et al.*, Ibersensor 2010, 9-11 November 2010, Lisbon, Portugal
- [19] S. R. Bhattacharyya, R. Ayouchi, M. Pinnisch *et al.*, Phys. Status Solidi C 9, 469 (2012)

- [20] K. Toyoura, H. Tsujimura, T. Goto *et al.*, Thin Solid Films 492, 88 (2005)
- [21] D. Cannavo, G. Knopp, P. Radi *et al.*, J. of Molecular Structure 782, 67 (2006)
- [22] S. T"Uzemen, H. Kavak, R. Esen, Chin. Phys.Lett. 24, 3477 (2007)
- [23] D. Wang, Y.C. Liu, J., Phys. Condens. Matter 16, 4635 (2004)
- [24] N. Jiang, D. G. Georgiev, A. H. Jayatissa *et al.*, J. Phys. D: Appl. Phys. 45, 135101 (2012)
- [25] C. García Núñez , J.L. Pau, M.J. Hernández *et al.*, Thin Solid Films 520, 1924 (2012)
- [26] J. M. Khoshman, N. Peica, C. Thomsen *et al.*, Thin Solid Films 520, 7230 (2012)
- [27] N. Jiang, D. G. Georgiev, T. Wen, A. H. Jayatissa, Thin Solid Films 520, 1698 (2012)
- [28] A. H. Jayatissa, T. Wen, M. Gautam, J. Phys. D: Appl. Phys. 45, 045402 (2012)
- [29] M. Futsuhara, K. Yoshioka, O. Takai, Thin Solid Films 322, 274 (1998)
- [30] E. Aperathitis, V. Kambilafka, M. Modreanu, Thin Solid Films 518, 1036 (2009)
- [31] F. Zong, H. Ma,W. Du, J. Ma, X. Zhang, H. Xiao *et al.*, Appl. Surf. Sci. 252 7983 (2006)
- [32] T. Wen, M. Gautam *et al.*, Materials Science in Semiconductor Processing 16, 318 (2013)
- [33] C. García Núñez, J. L. Pau, M. J. Hernandez *et al.*, Appl. Phys. Lett. 99, 232112 (2011)
- [34] Powder Diffraction File compiled by the Joint Committee on Powder Diffraction, Card No. 10-0256
- [35] Powder Diffraction File compiled by the Joint Committee on Powder Diffraction, Card No. 4-0831
- [36] V. Kambilafka, P. Voulgaropoulou, S. Dounis, Thin Solid Films 515, 8573 (2007)
- [37] L. Kubler, Haug, E. K. Hlil, D Bolmont *et al.*, J. Vac. Sci. Technol. A 5, 2323 (1986)
- [38] C. Palacio, J. M. Sanz, J. M. Martinez-Duart, Thin Solid Films 124, 243 (1985)
- [39] S. J. Pearton *et al.*, Superlattices and Microstructures 34, 3 (2004)
- [40] Powder Diffraction File compiled by the Joint Committee on Powder Diffraction, Card No. 3-0752
- [41] S.M. Sze, "Semiconductor Devices Physics and Technology", 3rd edition, Wiley (1985)
- [42] B.G. Streetmam, S.K. Banerjee, "Solid State Electronic Devices", 6th edition, Prentice Hall (2006)
- [43] M. Krishna K, Synthesis and Characterisation of Zinc Gallate Based Phosphors for Thin Film Electroluminescent Devices, PhD Thesis (2008)
- [44] D. Ginley, H. Hosono, D. Paine, "Handbook of Transparent Conductors", Springer (2011)
- [45] F Litimein, B Bouhafs, Z Dridi, P Ruterana, New Journal of Physics 4, 64.1 (2002)

[46] E. Fortunato, P. Barquinha, R. Martins, *Advanced Materials* (2012)

[47] Y. Ye, R. Lim, J. M. White, *J. App Phys* 106, 074512 (2009)

[48] D. Schroder, "Semiconductor Material and Device Characterization", Wiley & Sons (1990)

[49] J. Tauc, R. Grigorvici, A. Vancu, *Phys. Status Solidi* 15, 627 (1966)